50th AIAA Aerospace Sciences Meeting including the New Horizons Forum and Aerospace Exposition
09 - 12 January 2012, Nashville, Tennessee

AIAA 2012-0457

50th AIAA Aerospace Sciences Meeting and Exhibit, January 9-12, 2012, Nashville, TN

Robust Computation of Turbulent flows using a Discontinuous Galerkin Method

Nicholas K. Burgess *
and
Dimitri J. Mavriplis †
Department of Mechanical Engineering, University of Wyoming, Laramie WY 82071, USA

This work considers the development of a robust discontinuous Galerkin (DG) solver for turbulent aerodynamic flows using the turbulence model of Spalart and Allmaras (SA). Previous work on this subject has demonstrated that applying DG discretizations to turbulent flows can be difficult, due to robustness issues related to non-smooth behavior of the turbulence model variable (or variables). This work presents two options for enhancing solver robustness. The first consists of employing a finite volume discretization with a first-order accurate convection term for the turbulence model, which is a standard practice in the low-order methods context. Computational results show that despite the first-order accurate discretization of the turbulence model there is still benefit to using higher-order discretizations for the mean flow equations and at the very least, discontinuous Galerkin solutions to the Reynolds Averaged Navier-Stokes (RANS) equations are obtained robustly. The second method of robustness enhancement considers modifications to the turbulence model equation. Numerical experiments have shown that the modifications to the turbulence model equation employed in this work are particularly effective at increasing solver robustness. Both robustness enhancement methods are applied to realistic aerodynamic flows including a subsonic turbulent airfoil flow and high-lift configurations at high angles of attack.

I. Introduction

Discontinuous Galerkin (DG) methods are capable of generating high-order accurate solutions to the Euler and Navier-Stokes equations.[1–6] However, high-order accuracy is usually only attained if the solution is smooth. Unfortunately, for aerodynamic applications solutions are rarely smooth. The most pressing source of non-smooth behavior for Reynolds-averaged Navier-Stokes (RANS) solutions is associated with the turbulence models used to close the mean flow equations. When employing high discretization orders the turbulence model of Spalart and Allmaras develops a discontinuity in its working variable at the interface between turbulent/non-turbulent regions of the flow. This phenomena is now well known and has been reported by various researchers[7–9] including previous work by the authors.[10] This discontinuity results in oscillatory high-order solutions, which can easily cause solver failure due to the appearance of unphysical negative working variable values. This is especially true for high-lift configurations where particularly large magnitude negative values may be generated. However, discretization error remains a dominant concern in the solution of turbulent aerodynamic flows, as demonstrated in the AIAA drag prediction workshop series.[11,12] Furthermore, it is well known that one of the most effective methods for removing discretization error is to increase the order of accuracy of the spatial discretization.[13–18] Therefore competing interests exist for the computation of turbulent flows. On one hand, additional accuracy is required, and on the other hand, high-order discretizations of the turbulence model equations are unstable. Hence the primary goal of this work is to examine robustness enhancement strategies for high-order accurate discretizations of turbulent flows using the Reynolds Averaged Navier-Stokes (RANS) equations. The robustness of the current solver will be demonstrated through challenging test cases that are relevant to aerodynamic applications.

Although the use of high-order accurate discretizations for RANS problems is not commonplace, there are several examples of successful high-order DG RANS solutions using standard turbulence models in the literature.[10,15,19–21] The current solver using a DG discretization of the unmodified Spalart-Allmaras (SA) turbulence model[22] has been

*Graduate Research Assistant, Department of Mechanical Engineering, University of Wyoming, AIAA Student Member

†Professor, Department of Mechanical Engineering, University of Wyoming, AIAA Associate Fellow

able to replicate almost all the results of these references, however not as robustly as is required for production use. Many production level solvers such as, CFL3D,[23] FUN3D,[24] and NSU3D[25] use discretizations of the turbulence model equations with first-order accurate convection terms for the turbulence model. Moreover, Spalart and Allmaras use this discretization in their original formulation of the one-equation SA model.[22] Borrowing from this idea, the first approach taken in this work consists of coupling the current DG solver for the mean flow equations with a finite-volume discretization of the SA turbulence model. Furthermore, it has been determined that even with first-order accurate convection terms in the turbulence model, sufficient levels of eddy viscosity are produced so that the model adequately captures turbulent flow physics. This is true provided that the appropriate convective numerical flux formulation is used. High-order methods are implemented for the mean flow equations in order to remove as much discretization error from the mean flow equations as possible. This combined discretization approach is denoted as the hybrid discretization approach. The hybrid discretization approach allows for some interesting investigations of the relationship between the discretization order of the mean flow and turbulence model equations.

There have been several attempts at stabilizing high-order solutions of the turbulence model equations.[7, 10, 20] These stabilization methods attempt to remove the non-smooth behavior from the discrete solution of the turbulence model equation in the same fashion that shock waves are stabilized using limiters or artificial diffusion. Unfortunately, all of these methods have proven unsatisfactory in some way, either the method allows for negative eddy viscosity values or compromises solution accuracy.

As an alternative approach to preventing solver failure due to turbulence model non-smooth behavior, reference[15] has introduced modifications to the SA turbulence model equation designed to alleviate the difficulties of solving this equation with high-order DG discretizations. Modifications are distinct from stabilization methods because modifications change the continuous SA turbulence model equation, whereas stabilization methods attempt to modify the non-smooth behavior of the discrete solution. Modifications to the turbulence model source term designed to prevent negative eddy viscosity values have been proposed in reference.[15] These have been implemented in the current work but have not been found to increase solver robustness sufficiently. An alternate approach is taken in the recent modifications proposed in reference.[9] Rather than attempting to prevent negative values, the approach of reference[9] defines an auxiliary variable that is always positive and forces the model into a convection only equation when negative values occur. This approach is particularly effective because the source and diffusion terms are the causes of instability when the turbulence model working variable becomes negative. In the current work, the modification proposed in reference[9] is combined with the production term modification of reference.[15] Additionally, a fully coupled convective flux function for the RANS-SA system of equations is implemented, and a fully coupled Newton solver is used to drive the complete system of RANS equations to convergence. These additional modifications from the standard approach to SA turbulence model definition, discretization and solution are the key components for a robust high-order SA turbulence model solution procedure.

In this work, both the finite-volume and DG discretizations of the SA turbulence model equation are implemented and used in conjunction with a high-order DG discretization of the mean flow equations. Both approaches are shown to be robust and the effect on the mean flow of discretizing the turbulence model to higher-order accuracy is examined in detail.

II. Governing Equations

The conservative form of the compressible Reynolds Averaged Navier-Stokes (RANS) equations describing the conservation of mass, momentum and total energy in two dimensions are given as:

$$\frac{\partial \mathbf{u}}{\partial t} + \nabla \cdot \left(\vec{\mathbf{F}}_c(\mathbf{u}) - \vec{\mathbf{F}}_v(\mathbf{u}, \nabla \mathbf{u}) \right) = \mathbf{S}(\mathbf{u}, \nabla \mathbf{u}) \tag{1}$$

subject to the appropriate boundary and initial conditions within a domain Ω. In this work the RANS equations are coupled to the one equation turbulence model of Spalart and Allmaras (SA model)[22] with the modifications given in reference.[15] The equation for this model is given by:

$$\frac{\partial \rho \tilde{\nu}}{\partial t} + \nabla \cdot (\rho \tilde{\nu} \vec{v}) = c_{b_1} \tilde{S} \rho \tilde{\nu} + \frac{1}{\sigma} \left[\nabla \cdot \left((\mu + \rho \tilde{\nu}) \nabla \tilde{\nu} \right) + c_{b_2} \rho \nabla \tilde{\nu} \cdot \nabla \tilde{\nu} \right] - c_{w_1} \rho f_w \left(\frac{\tilde{\nu}}{d} \right)^2 \tag{2}$$

where $\tilde{S}$ is given according to

$$\tilde{S} = \begin{cases} S + \bar{S} & \bar{S} \geq -c_{v_2} S \\ S + \frac{S\left(c_{v_2}^2 S + c_{v_3} \bar{S}\right)}{\left(c_{v_3} - 2c_{v_2}\right) S - \bar{S}} & \bar{S} \leq -c_{v_2} S \end{cases} \tag{3}$$

$$
\begin{aligned}
S &= \sqrt{\vec{\omega}\cdot\vec{\omega}} \\
\bar{S} &= \frac{\tilde{\nu}^2 f_{v_2}}{\kappa^2 d^2}
\end{aligned}
\tag{4}
$$

where $\vec{\omega}$ is the vorticity vector. The constants and functions f_{v_1}, f_{v_2} are the same as those in reference.[22] The additional constant c_{v_3} is given as $c_{v_3} = .9$. The above represents a conservative version of the turbulence model given in reference.[22] The state vector and flux vectors including those of the SA model equation for two-dimensional flow are explicitly given as:

$$
\mathbf{u} = \begin{Bmatrix} \rho \\ \rho u \\ \rho v \\ E_t \\ \rho\tilde{\nu} \end{Bmatrix}, \quad
\mathbf{F_c}^x = \begin{Bmatrix} \rho u \\ \rho u^2 + P \\ \rho uv \\ u(E_t + P) \\ \rho u\tilde{\nu} \end{Bmatrix}, \quad
\mathbf{F_c}^y = \begin{Bmatrix} \rho v \\ \rho uv \\ \rho v^2 + P \\ v(E_t + P) \\ \rho v\tilde{\nu} \end{Bmatrix},
$$

$$
\mathbf{F_v}^x = \begin{Bmatrix} 0 \\ \tau_{xx} \\ \tau_{xy} \\ u\tau_{xx} + v\tau_{xy} + c_p\left(\frac{\mu}{Pr} + \frac{\mu_T}{Pr_T}\right)\frac{\partial T}{\partial x} \\ \frac{1}{\sigma}(\mu + \rho\tilde{\nu})\frac{\partial\tilde{\nu}}{\partial x} \end{Bmatrix}, \quad
\mathbf{F_v}^y = \begin{Bmatrix} 0 \\ \tau_{yx} \\ \tau_{yy} \\ u\tau_{yx} + v\tau_{yy} + c_p\left(\frac{\mu}{Pr} + \frac{\mu_T}{Pr_T}\right)\frac{\partial T}{\partial y} \\ \frac{1}{\sigma}(\mu + \rho\tilde{\nu})\frac{\partial\tilde{\nu}}{\partial y} \end{Bmatrix},
\tag{5}
$$

$$
\mathbf{S} = \begin{Bmatrix} 0 \\ 0 \\ 0 \\ 0 \\ c_{b_1}\tilde{S}\rho\tilde{\nu} + \frac{1}{\sigma}\left[c_{b_2}\rho\nabla\tilde{\nu}\cdot\nabla\tilde{\nu}\right] - c_{w_1}\rho f_w\left(\frac{\tilde{\nu}}{d}\right)^2 \end{Bmatrix}
$$

where ρ is fluid density, ($\vec{u} = (u, v)$) are the Cartesian velocity components, P is the fluid pressure, E_t is the total energy, c_p is the specific heat at constant pressure, T is the fluid temperature, P_r and P_{r_T} are the Prandtl and turbulent Prandtl numbers respectively and τ_{ij} is the total viscous stress tensor including the Boussinesq approximated Reynolds stresses. Assuming a Newtonian fluid and using the Boussinesq approximation for the Reynolds stresses, the viscous stress tensor takes the form (with $x_i = x, y; \quad i = 1, 2$):

$$
\begin{aligned}
&\tau_{ij} = 2(\mu + \mu_T)S_{ij} \\
&S_{ij} = \frac{1}{2}\left(\frac{\partial u_i}{\partial x_j} + \frac{\partial u_j}{\partial x_i}\right) - \frac{1}{3}\frac{\partial u_k}{\partial x_k}\delta_{ij} \\
&\text{for } i = 1, 2,\ j = 1, 2
\end{aligned}
\tag{6}
$$

where μ is the fluid viscosity obtained via Sutherland's law and μ_T is a turbulent eddy viscosity, which is given by:

$$
\begin{aligned}
\mu_T &= \begin{cases} \rho\tilde{\nu} f_{v_1} & \tilde{\nu} \geq 0 \\ 0 & \tilde{\nu} < 0 \end{cases} \\
f_{v_1} &= \frac{\left(\frac{\rho\tilde{\nu}}{\mu}\right)^3}{\left(\frac{\rho\tilde{\nu}}{\mu}\right)^3 + c_{v_1}^3} \\
c_{v_1} &= 7.1
\end{aligned}
\tag{7}
$$

The components of the viscous stress tensor for two dimensional flow are given explicitly as:

$$
\begin{aligned}
&\tau_{xx} = (\mu + \mu_T)\left(\frac{4}{3}\frac{\partial u}{\partial x} - \frac{2}{3}\frac{\partial v}{\partial y}\right), \quad \tau_{xy} = (\mu + \mu_T)\left(\frac{\partial u}{\partial y} + \frac{\partial v}{\partial x}\right) \\
&\tau_{yx} = (\mu + \mu_T)\left(\frac{\partial u}{\partial y} + \frac{\partial v}{\partial x}\right), \quad \tau_{yy} = (\mu + \mu_T)\left(\frac{4}{3}\frac{\partial v}{\partial y} - \frac{2}{3}\frac{\partial u}{\partial x}\right)
\end{aligned}
\tag{8}
$$

It should be understood that all quantities in the above equations are the Reynolds Averaged quantities (the usual $\bar{()}$ notation is omitted for simplicity). The pressure is obtained from the ideal gas equation of state given as:

$$P = (\gamma - 1)\left[E_t - \frac{1}{2}\rho\left(u^2 + v^2\right)\right] \tag{9}$$

where $\gamma = 1.4$ is the ratio of specific heats.

III. Spatial Discretization

III.A. Discontinuous Galerkin Discretization

In this work the spatial discretization of reference[16] is used for the mean flow equations. The turbulence model is either discretized using the same DG discretization or alternatively is discretized using a finite-volume approach as described in Section III.B.

Let the computational domain Ω be partitioned into a set of non-overlapping elements denoted $\mathcal{T}_{h,p}$, where h and p are the "size" and "order" of the elements of $\mathcal{T}_{h,p}$. Subsequently we will omit the subscript p in the notation for brevity and just let $\mathcal{T}_h$ represent the discretized domain. The discontinuous Galerkin discretization is given by finding $\mathbf{u}_h \in \mathcal{V}_h^p$ such that

$$\sum_{k\in\mathcal{T}_h}\int_{\Omega_k}\mathbf{v}_h^T\frac{\partial\mathbf{u}_h}{\partial t} + \mathbf{v}_h^T\nabla\cdot\left(\vec{\mathbf{F}}_c\left(\mathbf{u}_h\right) - \vec{\mathbf{F}}_v\left(\mathbf{u}_h,\nabla\mathbf{u}_h\right) - \vec{\mathbf{F}}_{ad}\left(\varepsilon,\mathbf{u}_h,\nabla\mathbf{u}_h\right)\right) - \mathbf{v_h}^T\mathbf{S}\left(\mathbf{u}_h,\nabla\mathbf{u}_h\right)d\Omega_k = 0, \quad \forall\mathbf{v}_h \in \mathcal{V}_h^p \tag{10}$$

where $\mathbf{v}_h$ represents an element basis or test function and $\mathbf{u}_h$ denotes the discretized form of the solution vector which is expanded in terms of the basis functions. The above equation can be written as

$$\sum_{k\in\mathcal{T}_h}\int_{\Omega_k}\mathbf{v}_h^T\frac{\partial\mathbf{u}_h}{\partial t}d\Omega_k + \mathbf{R}_h\left(\mathbf{u}_h,\nabla\mathbf{u}_h,\mathbf{v}_h\right) = 0, \quad \forall\mathbf{v}_h \in \mathcal{V}_h^p \tag{11}$$

where the $\mathbf{R}_h\left(\mathbf{u}_h,\nabla\mathbf{u}_h,\mathbf{v}_h\right)$ is the discrete spatial residual. The spatial residual is integrated by parts resulting in the following weak form

$$\begin{aligned}
\mathbf{R}_h\left(\mathbf{u}_h,\nabla\mathbf{u}_h,\mathbf{v}_h\right) = &-\sum_{k\in\mathcal{T}_h}\int_{\Omega_k}\nabla\mathbf{v}_h^T\cdot\left(\vec{\mathbf{F}}_c\left(\mathbf{u}_h\right) - \vec{\mathbf{F}}_v\left(\mathbf{u}_h,\nabla\mathbf{u}_h\right) - \vec{\mathbf{F}}_{ad}\left(\varepsilon,\mathbf{u}_h,\nabla\mathbf{u}_h\right)\right)\\
&+\mathbf{v_h}^T\mathbf{S}\left(\mathbf{u}_h,\nabla\mathbf{u}_h\right)d\Omega_k +\\
&\sum_{i\in I_h}\int_{\Gamma^i}\mathcal{H}_c\left(\mathbf{u}_h^+,\mathbf{u}_h^-,\vec{n}\right) - \mathcal{H}_v\left(\mathbf{u}_h,\mathbf{u}_h^-,\mathbf{w}_h^+,\mathbf{w}_h^-,\nabla\mathbf{u}_h^+,\nabla\mathbf{u}_h^-,\vec{n}\right) -\\
&\mathcal{H}_{ad}\left(\varepsilon^+,\varepsilon^-,\mathbf{u}_h^+,\mathbf{w}_h^+,\mathbf{w}_h^-,\mathbf{u}_h^-,\nabla\mathbf{u}_h^+,\nabla\mathbf{u}_h^-,\vec{n}\right)ds + \sum_{b\in\mathcal{B}_h}\int_{\Gamma^b}\mathcal{H}_c^b\left(\mathbf{u}_h^b\left(\mathbf{u}_h^+\right),\vec{n}\right) -\\
&\mathcal{H}_v^b\left(\mathbf{u}_h^b\left(\mathbf{u}_h^+\right),\mathbf{w}_h^+,\nabla\mathbf{u}_h^+,\vec{n}\right) - \mathcal{H}_{ad}^b\left(\varepsilon^+,\mathbf{u}_h^b\left(\mathbf{u}_h^+\right),\mathbf{w}^+,\nabla\mathbf{u}_h^+,\vec{n}\right)ds
\end{aligned} \tag{12}$$

where $\mathcal{H}_c(\cdot,\cdot,\cdot,\cdot,\vec{n})$ is the convective numerical flux, $\mathcal{H}_v(\cdot,\cdot,\cdot,\cdot,\cdot,\cdot,\vec{n})$ is the viscous numerical flux and $\mathcal{H}_{ad}(\cdot,\cdot,\cdot,\cdot,\cdot,\cdot,\cdot,\cdot,\vec{n})$ is the artificial diffusion numerical flux on the interior faces Γ^i. The numerical fluxes $\mathcal{H}_c^b(\cdot,\vec{n})$, $\mathcal{H}_v^b(\cdot,\cdot,\cdot,\vec{n})$ and $\mathcal{H}_{ad}^b(\cdot,\cdot,\cdot,\cdot,\vec{n})$ denote boundary numerical fluxes (which are different from the interior numerical fluxes) on a boundary edge Γ^b. The interior convective numerical flux is the approximate Riemann solver due to Roe.[26] The numerical fluxes for the viscous terms are obtained via a modified version of the symmetric interior penalty method (SIP) presented in reference,[16] which seeks to penalize the solution for being discontinuous at the element interfaces. For full details of the discretization, including SIP method details, see references.[16,27]

III.B. Finite-Volume Discretization of the Spalart Allmaras Turbulence Model

The first approach investigated for formulating a robust solution strategy for high-order DG RANS problems consists of coupling the spatial discretization of reference[16] described above applied to the mean flow equations with a finite-volume discretization of the SA turbulence model equation using first-order accurate convection terms (denoted as: finite-volume discretization). Unfortunately, by discretizing the turbulence model in this fashion, there is now a

resolution discrepancy between the mean flow equations and the turbulence model equation. This is inevitable for this type of hybrid methodology because DG methods couple the discretization order and number of degrees of freedom (DoFs) where finite-volume methods do not. In order to have a finite-volume representation and not reconstruct model variable gradients, the diffusive source term must be cast in a non-conservative form, as shown in reference.[22] The turbulence model is discretized on a mesh of elements $\mathcal{T}_{h,0}$ and the discrete solution is in the space of piecewise constant functions $\rho\tilde{\nu}_h \in \mathcal{V}_h^0$. Substitution of the discrete solution into the model equation given in Eq. (2) and integration over the domain yields.

$$\begin{aligned}&\sum_{k\in\mathcal{T}_h}\int_{\Omega_k}\left[\frac{\partial\rho\tilde{\nu}_h}{\partial t}+\frac{\partial\left(u_h\rho\tilde{\nu}_h\right)}{\partial x}+\frac{\partial\left(v_h\rho\tilde{\nu}_h\right)}{\partial y}-\frac{1}{\sigma}\nabla\cdot\left(\left(\mu_h+\rho\tilde{\nu}_h\right)\left(1+c_{b_2}\right)\nabla\tilde{\nu}_h\right)-\right.\\&\left.c_{b_2}\rho\tilde{\nu}_h\nabla^2\tilde{\nu}_h-S_h\right]d\Omega_k=0\\&\text{with}\\&S_h=c_{b_1}\tilde{S}\rho\tilde{\nu}-c_{w_1}\rho f_w\left(\frac{\tilde{\nu}}{d}\right)^2\end{aligned}\tag{13}$$

Integration by parts of Eq. (13) results in

$$\begin{aligned}&\sum_{k\in\mathcal{T}_h}\int_{\Omega_k}\frac{\partial\rho\tilde{\nu}_h}{\partial t}-S_h\left(\mathbf{u}_h,\nabla\mathbf{u}_h\right)d\Omega_k+\sum_{i\in I_h}\int_{\Gamma^i}\mathcal{H}_c\left(\mathbf{u}_h\right)-\left(\mathcal{H}_v\left(\mathbf{u}_h\right)\right)^{\pm}ds+\\&\sum_{b\in\mathcal{B}_h}\int_{\Gamma^b}\mathcal{H}_c^b\left(\mathbf{u}_h^b\left(\mathbf{u}_h^+\right)\right)+\mathcal{H}_v^b\left(\mathbf{u}_h^+,\mathbf{u}_h^b\left(\mathbf{u}_h^+\right)\right)ds=0\end{aligned}\tag{14}$$

where

$$\begin{aligned}&\mathcal{H}_c=\frac{1}{2}\left[\left(\tilde{u}_h\rho\tilde{\nu}_h\right)^+-\left(\tilde{u}_h\rho\tilde{\nu}_h\right)^-+max\left(\tilde{u}_h^+,\tilde{u}_h^-\right)\left(\rho\tilde{\nu}_h^+-\rho\tilde{\nu}_h^-\right)\right]\\&\tilde{u}_h=\left(u_hn_x+v_hn_y\right)\end{aligned}\tag{15}$$

$$\mathcal{H}_c^b=\left(\tilde{u}_h\rho\tilde{\nu}_h\right)^b\tag{16}$$

$\mathcal{H}_c$ is an upwind numerical flux function for a scalar convection equation and $\mathcal{H}_c^b$ is a boundary numerical flux function for a scalar convection equation. The numerical flux for the turbulence model equation diffusion term is taken as:

$$\begin{aligned}\left(\mathcal{H}_v\right)^+=&\left[\frac{1}{2}\left(\mu^++\mu^-+\left(\rho\tilde{\nu}^++\rho\tilde{\nu}^-\right)\left(1+cb_2\right)\right)-\rho\tilde{\nu}^+cb_2\right]\times\\&\left(\frac{\left(\tilde{\nu}^--\tilde{\nu}^+\right)\left(\Delta x^{\pm}\right)}{\left(l^{\pm}\right)^2}n_x+\frac{\left(\tilde{\nu}^--\tilde{\nu}^+\right)\left(\Delta y^{\pm}\right)}{\left(l^{\pm}\right)^2}n_y\right)\end{aligned}\tag{17}$$

with

$$\begin{aligned}\Delta x^{\pm}&=x^--x^+\\\Delta y^{\pm}&=y^--y^+\\l^{\pm}&=\sqrt{\Delta x^{\pm2}+\Delta y^{\pm2}}\end{aligned}\tag{18}$$

$$\begin{aligned}\left(\mathcal{H}_v\right)^-=&\left[\frac{1}{2}\left(\mu^++\mu^-+\left(\rho\tilde{\nu}^++\rho\tilde{\nu}^-\right)\left(1+cb_2\right)\right)-\rho\tilde{\nu}^-cb_2\right]\times\\&\left(\frac{\left(\tilde{\nu}^--\tilde{\nu}^+\right)\left(\Delta x^{\pm}\right)}{\left(l^{\pm}\right)^2}n_x+\frac{\left(\tilde{\nu}^--\tilde{\nu}^+\right)\left(\Delta y^{\pm}\right)}{\left(l^{\pm}\right)^2}n_y\right)\end{aligned}\tag{19}$$

$\mathcal{H}_v^{\pm}$ are simplified Laplacian viscous flux functions and are employed so that turbulence model gradients are not required. The same formulation of the turbulence model viscous flux is employed in[28] and is exact for orthogonal quadrilateral and equilateral triangle meshes. Similarly, the boundary viscous numerical flux is taken as:

$$\begin{aligned}\mathcal{H}_v^b=&\left[\frac{1}{2}\left(\mu^++\mu^b+\left(\rho\tilde{\nu}^++\rho\tilde{\nu}^b\right)\left(1+cb_2\right)\right)-\rho\tilde{\nu}^+cb_2\right]\times\\&\left(\frac{\left(\tilde{\nu}^b-\tilde{\nu}^+\right)\left(\Delta x^{\pm}\right)}{\left(l^{\pm}\right)^2}n_x+\frac{\left(\tilde{\nu}^b-\tilde{\nu}^+\right)\left(\Delta y^{\pm}\right)}{\left(l^{\pm}\right)^2}n_y\right)\end{aligned}\tag{20}$$

H_v^b is the boundary simplified Laplacian viscous numerical flux. These flux formulations treat the SA turbulence model equation as decoupled from the mean flow RANS equations.

The source term discretization is straight forward since it does not depend on the gradient of the turbulence model variable. While the convective discretization can be used with any numerical method, the diffusion discretization is specifically tailored for a finite-volume method. Additionally, the form of the continuous diffusion term used in this work is only advantageous for finite-volume and similar discretizations. This form of the diffusion term is not advantageous for DG discretizations because the manipulation used to obtain the non-conservative form of the diffusion term is undone upon integrating by parts to obtain a weak form DG discretization.

When employing this turbulence model discretization method, the turbulence model and mean flow equation discretizations occupy different function spaces, and a method by which to obtain $\mu^{\pm}$, $u_h^{\pm}$ etc. for use in the turbulence model discretization is required. Due to the finite-volume turbulence model discretization, an appropriate quadrature rule consisting of a single Gauss point is chosen for the integrations. For volume integrals the Gauss point is at the cell-center and for edge integrals the Gauss point is at the edge mid-point. Mean flow quantities are projected from their modal representations to these quadrature points directly. This amounts to a "reconstruction" of the mean flow variables but not the turbulence model variables since the turbulence model variables are constant over the cell in question. The combination of this finite-volume discretization for the turbulence model equation combined with a DG discretization of the mean flow equations is denoted as a hybrid discretization.

III.C. Convective Flux Discretization

Through numerical experimentation it has been found that the SA turbulence model is sensitive to the amount of artificial diffusion introduced by the convective flux discretization. The sensitivity is demonstrated by either the generation of negative values of the turbulence model working variable or low eddy viscosity production. On the one hand, high artificial diffusion values cause the eddy viscosity values to become inappropriately low so that the model does not adequately model turbulent physics. On the other hand, low artificial diffusion values result in the generation of negative turbulence model working variable $\tilde{\nu}$ values, by allowing the presence of the aforementioned non-smooth behavior or discontinuity in the turbulence model working variable, which in turn causes negative values of the turbulence model working variable, resulting in solver failure.

For simplicity the discussion of these effects is restricted to a single numerical example, namely the turbulent flow over a flat-plate at $M_\infty = .1$ and $Re = 10,000,000$. This discussion is restricted to this simple test case in order to avoid unsteady flow solutions in the presence of low eddy viscosity values. Two basic discretizations are compared for this flow. The first discretization is a $p = 1$ DG discretization that employs the approximate Riemann solver of Roe[26] for the convection terms of the fully coupled system of the mean flow and turbulence model equations. The second discretization is a $p = 1$ DG discretization for the mean flow combined with a finite-volume discretization with first-order accurate convection terms for the turbulence model, as described in Section III.B. Two convective numerical fluxes for the first-order discretization of the turbulence model are examined: an uncoupled upwind flux derived for the turbulence model alone, where the artificial diffusion has no acoustic component, and a Roe approximate Riemann solver which fully couples the artificial diffusion for the mean flow and turbulence model equations. Essentially the uncoupled upwind flux treats the turbulence model equation as through it is decoupled from the mean flow equations. However, the coupled Roe approximate Riemann solver treats the turbulence model equation by adding it as an additional governing PDE to the system of equations in Eq. (5) and re-derives the approximate Riemann solver for this new system of equations.[27] Figure 1(a) and Figure 1(b) depict the u-velocity and $\rho\tilde{\nu}$ profiles plotted versus y/c using all the turbulence model discretization options. These profiles are extracted at the mid-chord of the plate, $x/c = .5$ where c is the chord length of the plate.

One immediately notices that using a $p = 1$ DG discretization of the turbulence model equation results in oscillations at the boundary layer edge, which causes negative values of $\tilde{\nu}$. Contrarily, employing a finite-volume turbulence model convection discretization using the fully coupled Roe approximate Riemann solver for the convective numerical flux results in under production of the eddy viscosity. Additionally, this approach results in a highly inaccurate mean flow velocity profile as shown in Figure 1(a). The only presented turbulence model discretization option that provides sufficient eddy viscosity levels and remains positive throughout the domain is the first-order finite-volume discretization of the turbulence model convection term employing the uncoupled upwind flux Eq. (15). One should ask why the uncoupled upwind flux is not used in combination with a $p = 1$ DG discretization of the turbulence model and the answer is that the solver is unable to converge the turbulence model equation with this combination. The artificial diffusion supplied by this combination is insufficient to generate a stable discretization i.e. the negative SA working variable $\tilde{\nu}$ values have large magnitudes and cause solver failure.

Figure 2(a) and Figure 2(b) depict the same flow conditions computed using a second-order finite-volume solver.

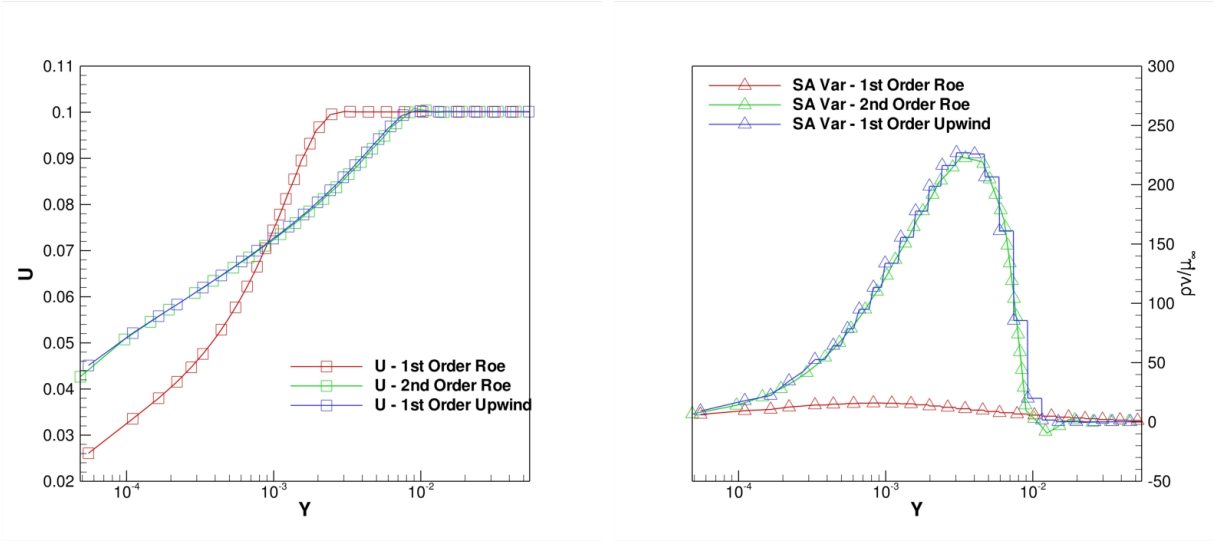

(a) u-velocity versus y/c (b) $\rho\tilde{\nu}/\mu_\infty$ versus y/c

Figure 1. Mid-chord profiles of u-velocity and working variable versus y/c for flow over flat-plate with $M_\infty = .1$, $Re = 10,000,000$, and $p = 1$ using a DG solver for the mean flow and various discretizations and convective numerical flux formulations for the turbulence model .

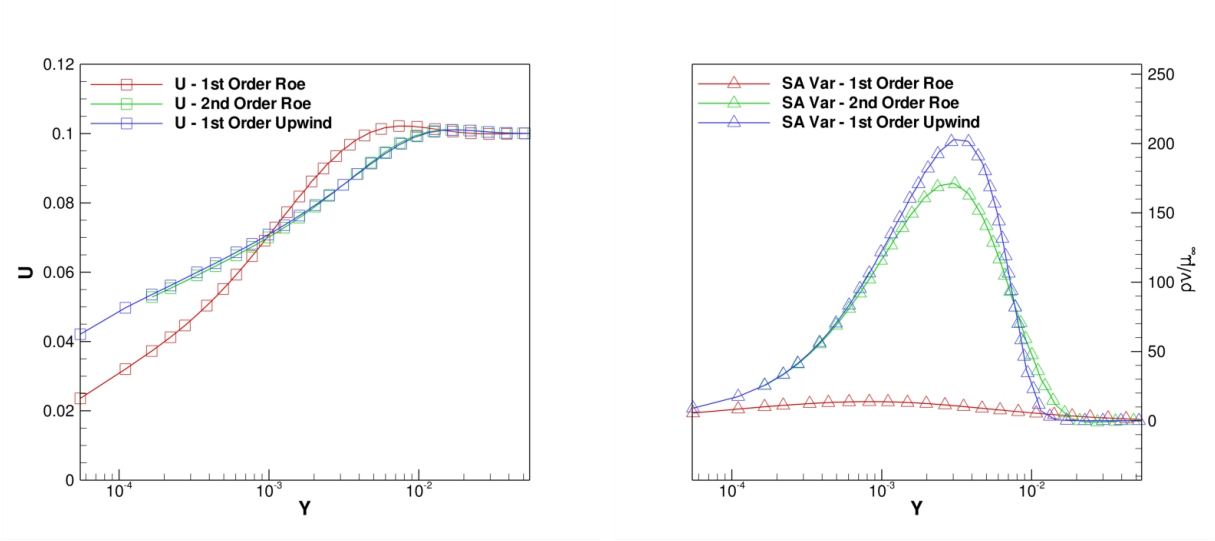

(a) u-velocity versus y/c (b) $\rho\tilde{\nu}/\mu_\infty$ versus y/c

Figure 2. Mid-chord profiles of u-velocity and working variable versus y/c for flow over flat-plate with $M_\infty = .1$, $Re = 10,000,000$ using a second-order finite-volume solver for the mean flow and various discretizations and convective numerical flux formulations for the turbulence model.

The finite-volume solver is capable of discretizing the mean flow equations using a second-order accurate finite-volume method based on a weighted least-square gradient reconstruction.[29] This discretization has also been implemented for the turbulence model equation in this finite-volume solver. In this case the second-order finite-volume discretization of the turbulence model convection term employs a min-mod limiter, the application of which was found to be necessary in order to obtain a converged solution. Additionally, the finite-volume solver is also able to discretize the turbulence model equation using the first-order convection term discretization described in Section III.B. Figure 2(b) demonstrates that the second-order finite-volume turbulence model convection discretization produces a small oscillation at the edge of the boundary layer, despite the use of the min-mod limiter in these computations, and the oscillation results in negative values of the SA working variable locally. Furthermore, the presence of the limiter has affected the peak value of the eddy viscosity, which is 16% lower than the finite-volume discretization employing the upwind flux. Thus the second-order turbulence model convection discretization is just as unsatisfactory in the finite-volume context as in the DG context, even with the use of the min-mod limiter. The second-order finite-volume turbulence model discretization results show the same trend as the $p = 1$ DG turbulence model discretization results. Hence, these issues appear in both DG and finite-volume discretization methods on unstructured grids.

Two conclusions can be drawn from this simple test. First of all, the SA turbulence model is sensitive to the amount of artificial diffusion that is applied through the convective flux discretization, which is affected both by the discretization order and the form of the discrete convective flux function. In particular, coupling the turbulence model and mean flow convective flux discretization at low-order results in a numerical scheme with excessive artificial diffusion and thus the model does not produce sufficient eddy viscosity. However, experiments for scalar convection problems with high-order DG discretizations have demonstrated that coupling the convective numerical flux between the equations controlling the mean flow and passive advecting scalar is necessary to achieve positive and smooth scalar values, for smooth initial conditions of the scalar. These two conclusions are at odds with one another, leaving few options for discretizing the turbulence model equation to high-order accuracy. Furthermore, the optimal combination of convective term discretization for the unmodified turbulence model has been found to be a first-order convection discretization employing an uncoupled upwind flux formulation (i.e a numerical flux where the sound speed does not appear in the artificial diffusion term for the turbulence model). Unfortunately it seems any second or higher-order convection discretization will not guarantee positive values of $\tilde{\nu}$, regardless of the discretization employed.

IV. An Effective Modification of the SA Turbulence Model

The previous analysis of the discretization of the turbulence model equation has shown that eliminating negative values that result from the non-smooth behavior of the turbulence model equation is difficult at best. An alternative approach to robustly accommodate the negative values of the turbulence model working variable is to consider modifying the turbulence model equation, such that negative values do not cause instability. Reference[15] details modifications to the source and diffusion terms of the turbulence model, which are designed to alleviate the difficulties encountered when the turbulence model working variable becomes negative. However, these modifications were not found to enhance robustness sufficiently in this work.

Recently, a new development in the modification of the SA turbulence model equation has been put forth in reference.[9] This modification does not attempt to remove the negative values of $\tilde{\nu}$, and as such high magnitude negative values may be present in the final solution of the turbulence model equation. However, the modified turbulence model becomes insensitive to the negative values through the introduction of an auxiliary variable that is constrained to remain positive. In the current work, we combine the turbulence model modifications developed in reference[9] with those of reference.[15] The modified turbulence model introduces the auxiliary variable ψ and is given as:

$$\frac{\partial \rho\tilde{\nu}}{\partial t} + \nabla\cdot(\rho\tilde{\nu}\vec{v}) = c_{b_1}\tilde{S}\rho\nu\psi + \frac{1}{\sigma}\left[\nabla\cdot\left(\left(\mu+\rho\nu\psi\right)\nabla\tilde{\nu}\right) + c_{b_2}\rho\nabla\tilde{\nu}\cdot\nabla\tilde{\nu}\right] - c_{w_1}\rho f_w\left(\frac{\nu\psi}{d}\right)^2 \tag{21}$$

The production term components are given by:

$$\begin{aligned}
\tilde{S} &= \begin{cases} S+\bar{S} & \bar{S} \geq -c_{v_2}S \\ S + \frac{S\left(c_{v_2}^2 S + c_{v_3}\bar{S}\right)}{\left(c_{v_3}-2c_{v_2}\right)S-\bar{S}} & \bar{S} \leq -c_{v_2}S \end{cases} \\
S &= \sqrt{\vec{\omega}\cdot\vec{\omega}} \\
\bar{S} &= \frac{\nu\psi f_{v_2}}{\kappa^2 d^2}
\end{aligned} \tag{22}$$

$$
\begin{aligned}
f_{v_1} &= \frac{\psi^3}{\psi^3 + c_{v_1}^3} \\
f_{v_2} &= 1 - \frac{\psi}{1 + \psi f_{v_1}}
\end{aligned}
\tag{23}
$$

and the destruction term coefficients are given by:

$$
\begin{aligned}
r &= \frac{\nu\psi}{\tilde{S}\kappa^2 d^2} \\
g &= r + c_{w_2}\left(r^6 - r\right) \\
f_w &= g\left[\frac{1 + c_{w_3}^6}{g^6 + c_{w_3}^6}\right]^{1/6}
\end{aligned}
\tag{24}
$$

The constants c_v,c_w, and κ have not been altered from their original values given in reference.[22] This form of the turbulence model is identical to the original form with the exception that the variable $\chi = \frac{\tilde{\nu}}{\nu}$ has been replaced by ψ in most of the source term coefficients, as well as in the diffusion coefficient. The variable ψ is designed to remain positive regardless of the value of $\tilde{\nu}$ and is given by:

$$
\begin{aligned}
\psi &= \begin{cases} .05log\left(1.0 + e^{(20.0\chi)}\right) & \chi \leq 10.0 \\ \chi & \chi > 10.0 \end{cases} \\
\chi &= \frac{\tilde{\nu}}{\nu}
\end{aligned}
\tag{25}
$$

The use of the variable ψ proposed in reference[9] is simple to implement within an existing CFD solver and is also easy to differentiate for implicit solution techniques. The effect of the modification is to deactivate the production, destruction and diffusion terms of the turbulence model equation when $\tilde{\nu}$ becomes negative, effectively rendering it as a simple advection equation, which is unaffected by negative values of $\tilde{\nu}$. While employing the variable ψ in the model source terms comes directly from reference,[9] this reference does not use the modified form of $\tilde{S}$, which in the authors' experience provides addition robustness to the turbulence model equation in the positive $\tilde{\nu}$ regime. Furthermore, when discretizing the convection term, the current work considers the entire RANS-SA system and uses the approximate Riemann solver of Roe for the convective flux treatment of the fully coupled RANS-SA system.[27] While the modifications of reference[9] is an important part of the turbulence model robustness enhancement, the modified form of $\tilde{S}$ and the fully coupled convective flux treatment are equally important aspects of the robustness enhancement. Without all of these modifications the solver would not be able to achieve the results presented in this work.

V. Implicit Solution Techniques: Algebraic Coupling

In addition to stable discretizations, efficient and robust solution techniques are required for the development of a robust production level aerodynamic DG solver. In this work, the RANS-SA system is solved using a damped fully implicit Newton solver that treats the mean flow and turbulence model equations in a fully coupled fashion.[10,27] The linear solver used at each Newton step is based on a line-implicit colored Gauss-Seidel (CGS) preconditioned GMRES solver.[27] The meshes employed for solving the RANS equations contain high aspect-ratio elements, which induce additional stiffness in the governing equations. An effective approach to alleviate this stiffness is to consider a line-implicit solver, which requires the construction of lines through an unstructured grid. The lines are constructed using a weighted graph approach.[10] A fully parallel Gauss-Seidel method requires that a coloring of the mesh be performed and lines are colored via a greedy algorithm that loops over all the lines formed for the line-implicit solver, assigning color integers to the lines. Once the lines have been colored, a block-tridiagonal solver is employed in a Gauss-Seidel fashion over the colors.

Constructing implicit solution techniques requires the determination of the flow Jacobian matrix. The flow Jacobian requires the differentiation of the residual $\mathbf{R}_h$ with respect to the discrete solution $\mathbf{u}_h$, a process known as linearization. Turbulence models are often linearized in a decoupled fashion i.e. turbulence models are linearized only with respect to the variables that the model equation controls. This results in a loosely coupled implicit solver formulation, that in many cases cannot fully converge the discrete equations. However, if the linearization is performed in a fully coupled fashion, it is far more likely that full convergence of the discrete equations can be achieved, at least

with the presented DG and finite-volume solvers. Full convergence of the discrete equations is especially important for high-order discretizations, since the magnitude of high-order modal coefficients can be very small.

A fully coupled linearization is obtained by differentiating the model equation with respect to every modal coefficient in the system of equations. For example, the turbulence model equation requires the molecular viscosity μ for the source and diffusion terms, which depends on all the mean flow quantities ρ, ρu, ρv, and E_t. Therefore, when linearizing the turbulence model there are off-diagonal coupling entries in the flux Jacobian matrix corresponding to differentiation with respect to the modal coefficients of the mean flow quantities.

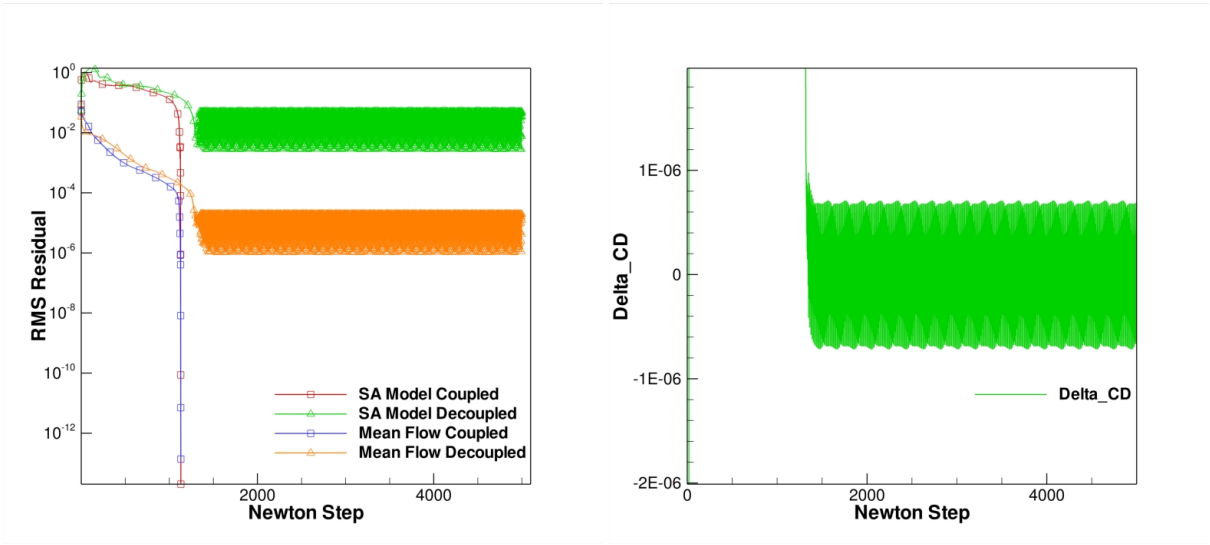

(a) Discrete flow equation residual history

(b) Computed drag difference

Figure 3. Comparison of coupled versus decoupled Jacobians on iterative convergence for turbulent flow over a flat-plate with $M_\infty = .1$ and $Re = 10,000,000$. The solution is obtained using the CGS preconditioned GMRES solver. The drag difference (right) is the difference between the fully converged flow solution computed drag value and the partially converged computed drag value, resulting from employing a decoupled Jacobian in the implicit solver.

Figure 3(a) depicts the iterative convergence using a colored Gauss-Seidel (CGS) preconditioned GMRES solver[27] for the turbulent flow over a flat-plate, employing a $p = 1$ DG discretization for the mean flow equations and the finite-volume discretization for the turbulence model equation, using both coupled and decoupled linearizations. Figure 3(a) shows that employing the decoupled flow Jacobian results in an implicit solver that cannot fully converge the discrete equation residuals to machine zero. However, employing the fully coupled flow Jacobian results in an implicit solver that fully converges both the turbulence model and mean flow equations without issue. Figure 3(b) depicts the difference between the drag value obtained by fully converging the discrete equations and the drag value computed using the partially converged decoupled flow Jacobian approach $\Delta C_D = |C_{Dcoupled} - C_{Ddecoupled}|$. Notice that the error in the computed drag value induced by partially converging the discrete equations i.e. $|C_{Dcoupled} - C_{Ddecoupled}|$ is approximately $\pm 5.0e-7$. Although the values of ΔC_D are small, values of this magnitude will often be insufficient for use with high-order methods where discretization errors are small. Therefore, a fully coupled Jacobian matrix is employed for all test cases in this work. It should be noted that the use of a fully coupled solution approach obviates the possibility of using various positivity preserving techniques at the non-linear or sub-iteration level as discussed for example in reference.[22] Therefore, this approach places additional importance in the formulation of a stable and realizable spatial discretization.

VI. Numerical Results: Hybrid Discretization

A DG solver that is capable of solving the RANS equations with a finite-volume discretization of the turbulence model is applied to several practical aerodynamic flows. The combination of a high-order DG discretization with a finite-volume discretization of the turbulence model equation with a first-order convection discretization is denoted as a hybrid discretization. The discretization of the turbulence model employed for all test problems is described Section III.B. Furthermore, negative values of the turbulence model working variable do not exist in the final steady-state solutions when the turbulence model is discretized with the finite-volume method. These cases are presented to illustrate the robustness of this approach and demonstrate that using a high-order DG discretization for the mean flow equations alone can still be beneficial for overall solution accuracy. All test cases are solved using the fully coupled

damped-Newton method with a line-implicit CGS preconditioned GMRES solver described above and detailed in reference.[27] For the mean flow equations the Riemann solver of Roe is employed as the convective flux function, whereas the convective flux function for the turbulence model is given in Eq. (15)

VI.A. Subsonic RAE2822 Airfoil

The first test case consists of the turbulent flow over an RAE2822 airfoil at $M_\infty = .4$, $\alpha = 2.79^o$, and $Re = 6,500,000$. The computational mesh employed for this test case is a mixed-element unstructured mesh containing $N = 5,980$ elements, with discretization orders ranging from $p = 1$ to $p = 4$. The computational mesh is depicted in Figure 4(a). The solution is converged using a line-implicit CGS preconditioned GMRES solver and each solution of discretization order p is initialized with a fully converged solution of discretization order $p-1$. Due to the finite-volume discretization of the turbulence model equation, increasing the discretization order p does not increase the number of unknowns of the turbulence model discretization i.e. turbulence model resolution remains fixed during p-enrichment.

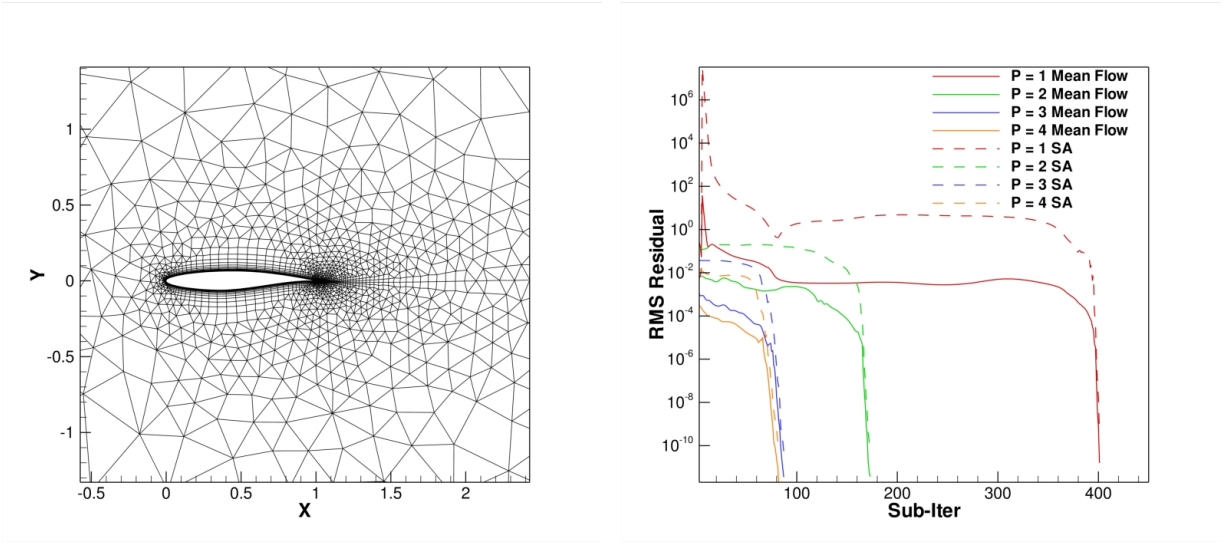

(a) Mesh $N = 5,980$ (b) Convergence history

Figure 4. Convergence history and mesh for subsonic flow over a RAE2822 airfoil at $M_\infty = .4$, $\alpha = 2.79^o$, and $Re = 6,500,000$ using discretization orders $p = 1$ to $p = 4$ for the mean flow and a first-order discretization for the turbulence model.

Table 1. Computed lift and drag coefficients for the RAE2822 airfoil with $M_\infty = .4$, $\alpha = 2.79^o$, and $Re = 6,500,000$ using $p = 1$ to $p = 4$.

p	NDoF	C_L	C_D
1	21,482	.536226	.016322
2	46,692	.553743	.008991
3	81,548	.554062	.008932
4	126,050	.553607	.008933

The convergence history for all discretization orders p is depicted in Figure 4(b), which shows that a fully converged solution is obtained for all discretization orders. The convergence rate is slower compared to laminar flow problems such as those in reference.[16] The slower convergence rate is due to the Newton damping requirements imposed by the turbulence model source terms. However, once the turbulence model source term transient has passed, the solution proceeds rapidly to a fully converged state. Note that Figure 4(b) does not show the secondary transient that has been observed[10] when $\tilde{\nu}$ becomes negative. Figure 5(a) through Figure 6(b) depict the computed Mach number and normalized turbulence model working variable contours for a $p = 1$ and a $p = 4$ discretization respectively. Figure 7(a) illustrates the surface pressure distribution for discretization orders $p = 1$ to $p = 4$ and Figure 7(b) shows the computed surface skin friction profiles also for discretization orders $p = 1$ to $p = 4$. Note that as the discretization order is increased these profiles become smoother indicating that increasing discretization order results in enhanced solution accuracy. Also note that the non-smooth behavior in the computed skin friction profile is restricted to sharp corners where the geometry is non differentiable.

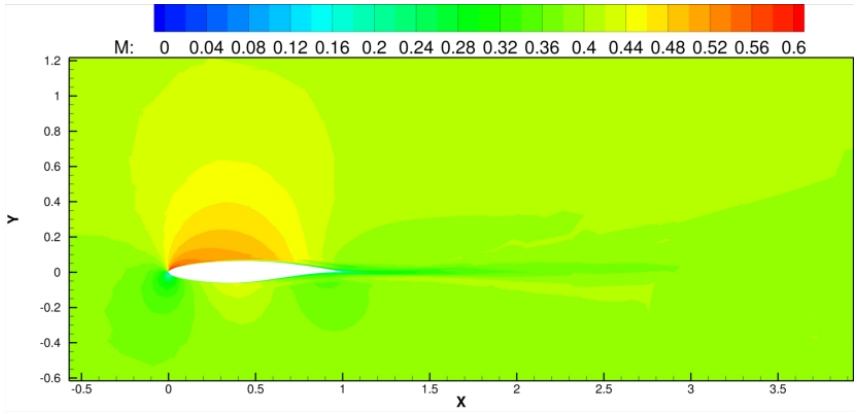

(a) Mach number contours, $p = 1$

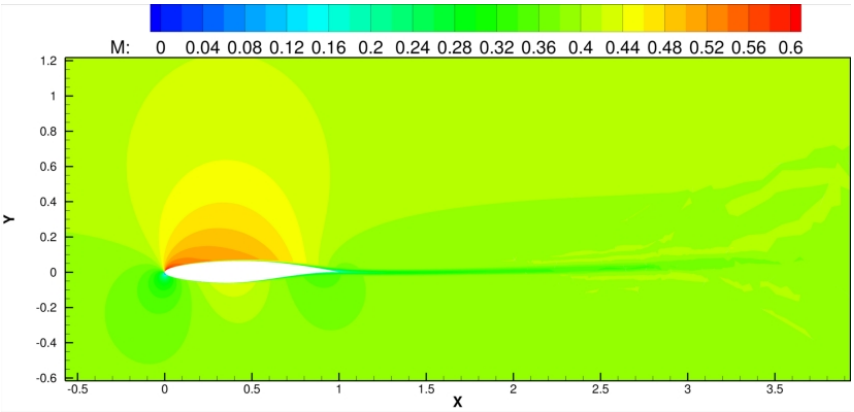

(b) Mach number contours, $p = 4$

Figure 5. Computed Mach number contours for subsonic flow over an RAE2822 airfoil at $M_\infty = .4$, $\alpha = 2.79^o$, and $Re = 6,500,000$.

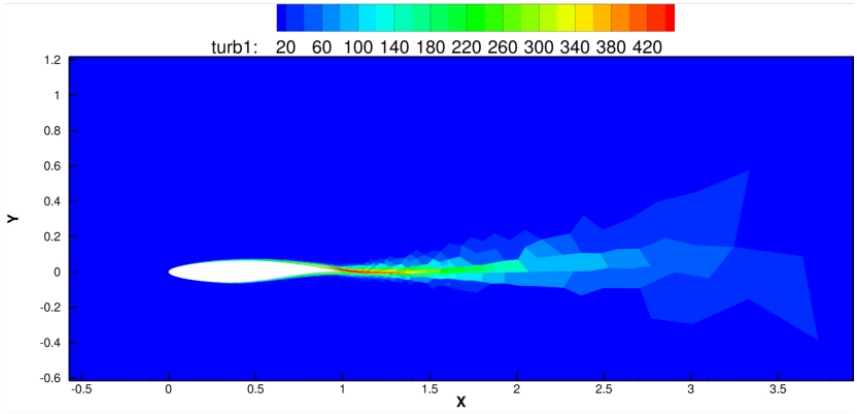

(a) $\rho\tilde{\nu}/\mu_\infty$ contours, $p = 1$

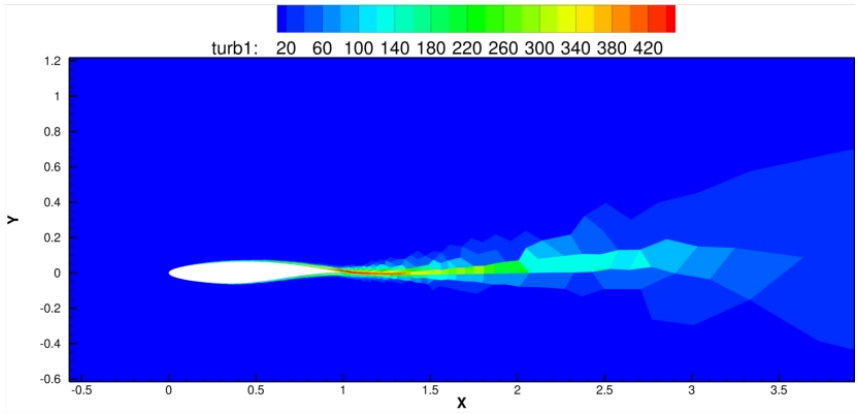

(b) $\rho\tilde{\nu}/\mu_\infty$ contours, $p = 4$

Figure 6. Computed $\rho\tilde{\nu}/\mu_\infty$ contours for subsonic flow over an RAE2822 airfoil using the Spalart Allmaras turbulence model at $M_\infty = .4$, $\alpha = 2.79^o$, and $Re = 6,500,000$ with mean flow discretization orders $p = 1$ and $p = 4$.

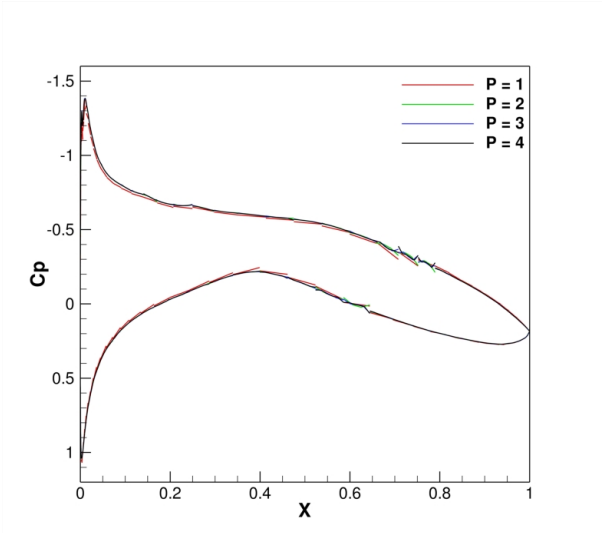

(a) Surface pressure coefficient

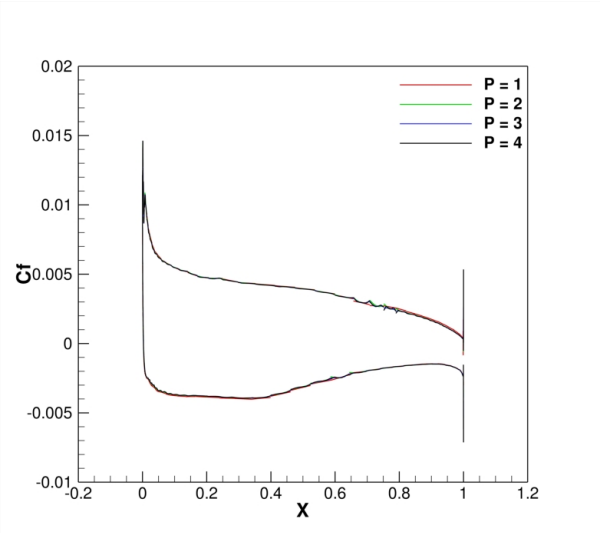

(b) Skin friction coefficient

Figure 7. Computed surface pressure coefficient and skin friction for subsonic flow over an RAE2822 airfoil using the Spalart Allmaras turbulence model at $M_\infty = .4$, $\alpha = 2.79^o$, and $Re = 6,500,000$ using $p = 1$ to $p = 4$.

Table 1 shows the discretization order p, N_{DoF}, computed lift and computed drag coefficients across the discretization order range. Table 1 shows that the computed drag coefficient has been resolved to .01 counts and the computed lift coefficient has been resolved to approximately 8 counts. As stated in the introduction, studying grid convergence is a primary target of this work and the results show that the solver is able to obtain grid converged results with respect to polynomial order changes and a fixed turbulence model resolution.

VI.B. High-lift Multi-element Airfoil Configuration L1T2

The second test case consists of the turbulent flow over the AGARD L1T2 high-lift multi-element airfoil configuration. The geometry consists of a three-element airfoil configuration and the flow conditions are $M = .197$, $\alpha = 20.18^o$, and $Re = 3,520,000$. The mesh employed for this test case is a mixed-element unstructured mesh with $N = 80,742$ elements as shown Figure 8. In this case, discretization orders ranging from $p = 1$ to $p = 3$ are employed. This case is presented in order to compare the DG results with experimental data provided by AGARD.

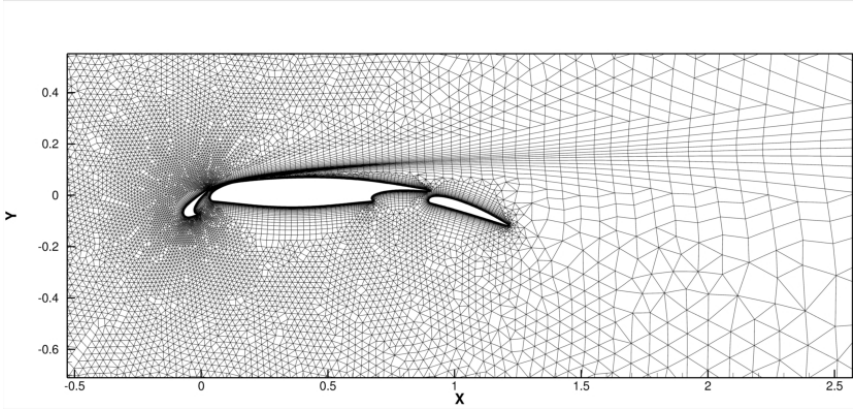

Figure 8. Computational mesh used for computing the flow around the AGARD L1T2 high-lift multi-element airfoil configuration at $M_\infty = .197$, $\alpha = 20.18^o$, and $Re = 3,520,000$.

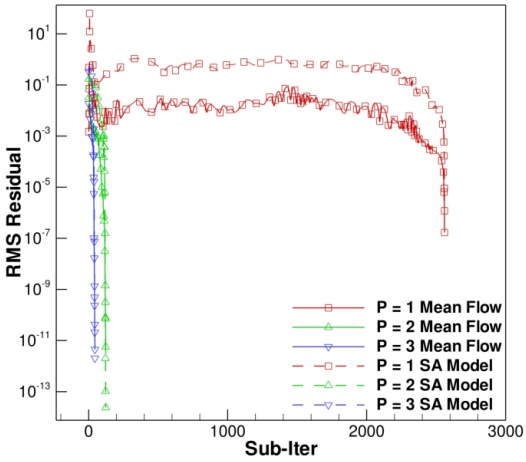

Figure 9. Convergence history of the flow around the AGARD L1T2 high-lift multi-element airfoil configuration at $M_\infty = .197$, $\alpha = 20.18^o$, and $Re = 3,520,000$.

Figure 9 depicts the iterative convergence of the flow solver and similarly to the previous RAE2822 airfoil test case, once the turbulence model transient has passed the solution converges rapidly to steady-state. Figure 10(a) through Figure 11(b) depict the Mach number and turbulence model working variable contours for a $p = 1$ and a $p = 3$ solution respectively. From the computed Mach number contours the flow is seen to approach sonic conditions on the slat leading-edge upper surface. The DG solver is robust enough to compute this flow without any form of artificial diffusion or limitation. Figure 12(a) shows a comparison between computed surface pressure coefficients and experimental values. The computed surface pressure coefficient results agree well with experimental values throughout

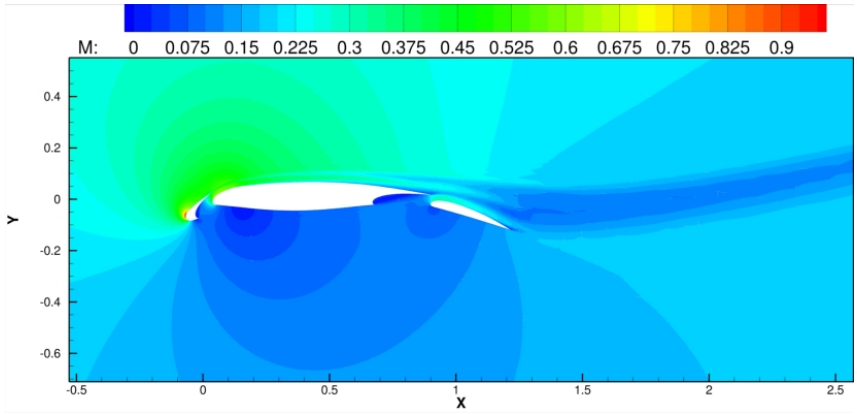

(a) Mach number contours at $p = 1$

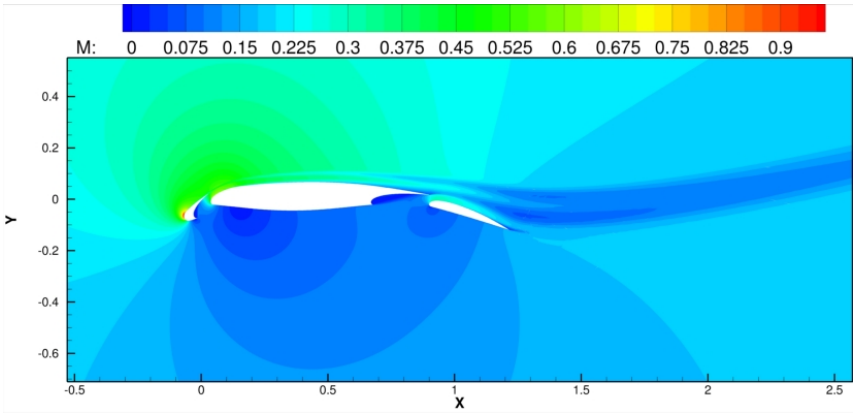

(b) Mach number contours at $p = 3$

Figure 10. Computed Mach number contours using a DG discretization with the Spalart-Allmaras turbulence model for flow over the AGARD L1T2 high-lift multi-element airfoil configuration with mean flow discretization orders $p = 1$ and $p = 3$, $M_\infty = .197$ and a first-order discretization for the turbulence model at $\alpha = 20.18^o$, and $Re = 3,520,000$.

Table 2. Computed lift and drag coefficients for the AGARD L1T2 multi-element airfoil configuration at $M_\infty = .197$, $\alpha = 20.18^o$, and $Re = 3,520,000$ using $p = 1$ to $p = 3$

p	NDoF	C_L	C_D
1	265,311	4.036398	.069400
2	553,707	4.012107	.068767
3	945,930	4.010951	.068340

the airfoil sections. Figure 12(b) depicts the computed skin friction coefficient using a $p = 3$ DG discretization for the mean flow equations and a smooth skin friction profile is obtained with the exception of the geometry slope discontinuities. Table 2 provides the numerical values of the computed lift and drag coefficients for each discretization order p. Table 2 shows that the computed drag coefficient is resolved to within 4 counts and the computed lift coefficient is resolved to within 11 counts. Figure 13(a) depicts the streamlines around the L1T2 multi-element airfoil configuration, showing the high flow incidence angle and high overall streamline curvature over the configuration. Figure 13(b) shows the streamlines near the slat for this case, illustrating the high streamline curvature in this region as the flow is accelerated around the leading edge of the slat and in the gap between the slat and main airfoil. Figure 13(c) shows the streamlines near the flap and flap cove on the main element showing a strong re-circulation region in the flap-cove. The DG solver displays no adverse robustness implications as a result of these smooth high gradient phenomena.

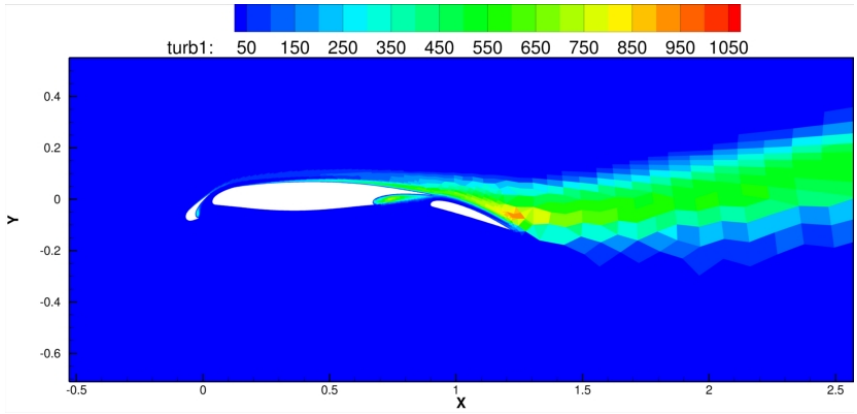

(a) $\rho\tilde{\nu}/\mu_\infty$ at $p = 1$

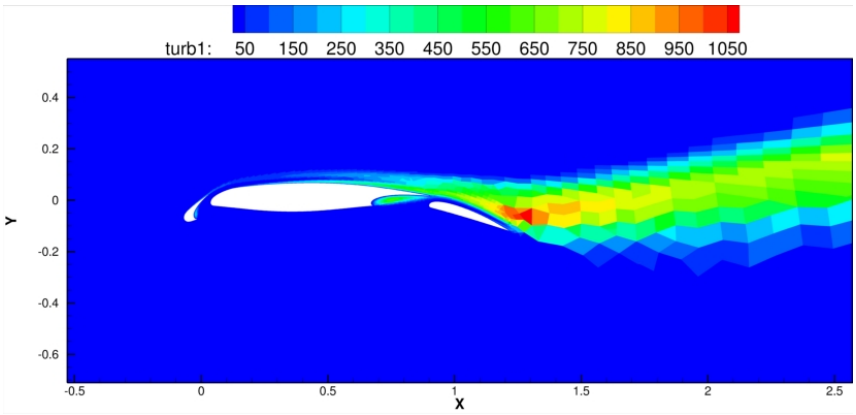

(b) $\rho\tilde{\nu}/\mu_\infty$ at $p = 3$

Figure 11. Computed $\rho\tilde{\nu}/\mu_\infty$ contours using the Spalart-Allmaras turbulence model for flow over the AGARD L1T2 high-lift multi-element airfoil configuration with mean flow discretization orders $p = 1$ and $p = 3$and a first-order discretization for the turbulence model at $M_\infty = .197$, $\alpha = 20.18^o$, and $Re = 3,520,000$.

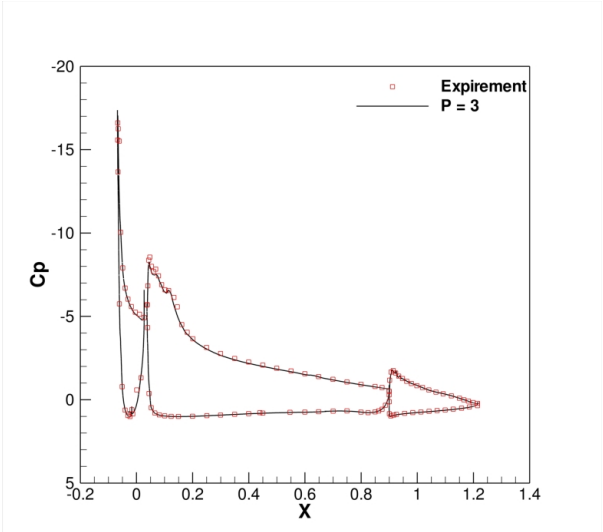

(a) Surface pressure coefficient at $p = 3$

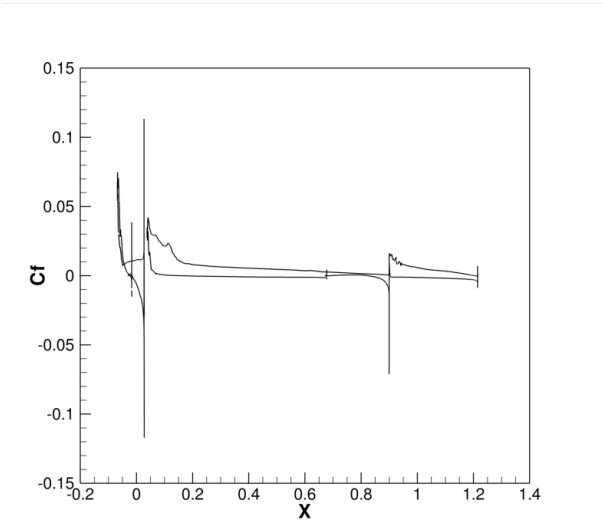

(b) Surface pressure coefficient at $p = 3$

Figure 12. Computed surface pressure and skin friction coefficients using the Spalart-Allmaras turbulence model for flow over the AGARD L1T2 high-lift multi-element airfoil configuration with a mean flow discretization order of $p = 3$, $M_\infty = .197$, $\alpha = 20.18^o$, and $Re = 3,520,000$.

VI.C. High-lift Multi-element Airfoil Configuration 30P30N

The third test case consists of the turbulent flow over a high-lift multi-element airfoil configuration denoted as the 30P30N configuration. The flow conditions for this test case are $M_\infty = .2$, $\alpha = 16^o$, and $Re = 9,000,000$. The

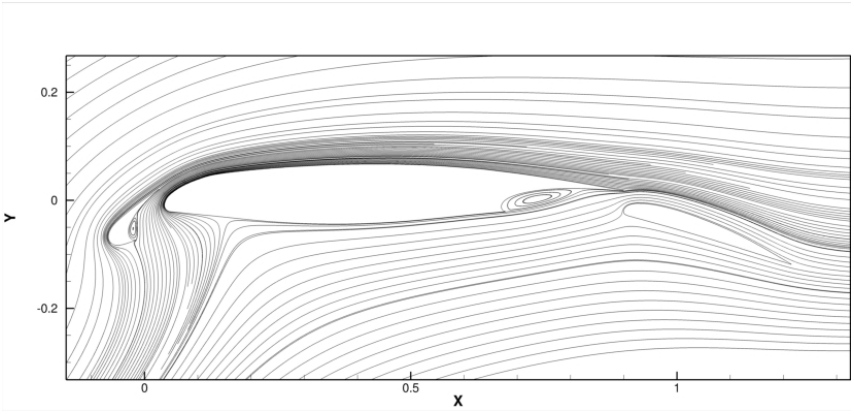

(a) Streamlines

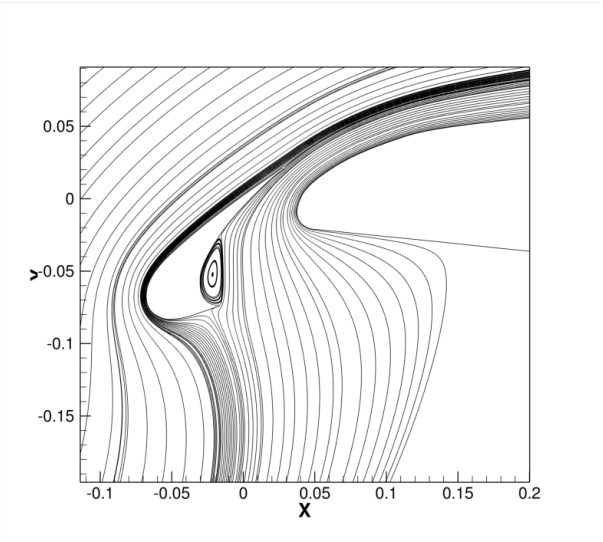

(b) Slat streamlines

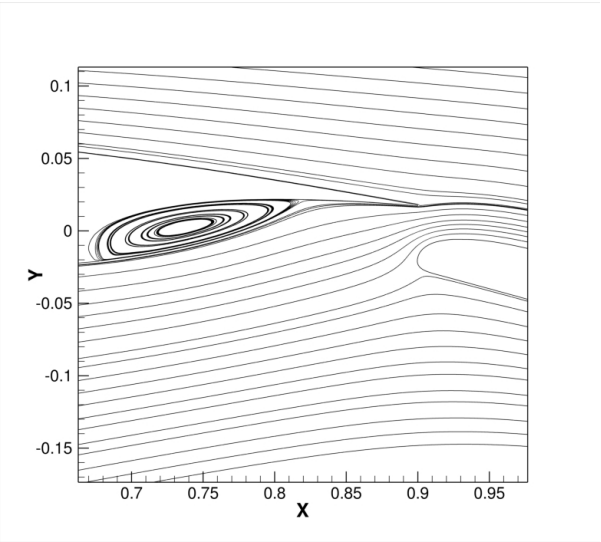

(c) Flap streamlines

Figure 13. Streamlines near the slat and flap using the Spalart-Allmaras turbulence model for flow over an L1T2 high lift multi-element airfoil with a mean flow discretization order of $p = 3$, $M_\infty = .197$, $\alpha = 20.18^o$, and $Re = 3,520,000$.

geometry for this test case consists of: a leading edge slat, a center or main element and a trailing edge flap, which are configured for a so-called landing configuration. The computational mesh employed for this case is a mixed-element unstructured mesh consisting of $N = 55,964$ elements shown in Figure 14.

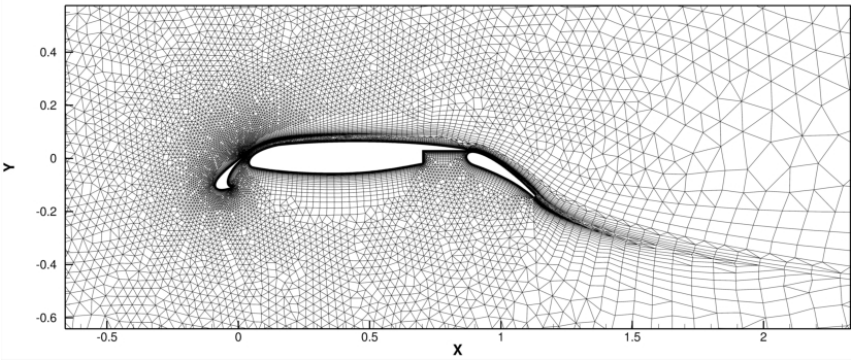

Figure 14. Mixed-element unstructured mesh used for computing flow around the 30P30N high-lift multi-element airfoil configuration at $M_\infty = .2$, $\alpha = 16^o$, and $Re = 9,000,000$.

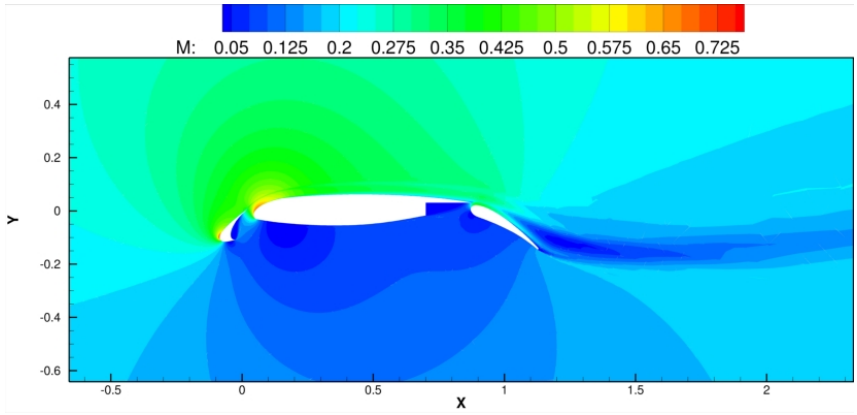

(a) Mach number contours, $p = 1$

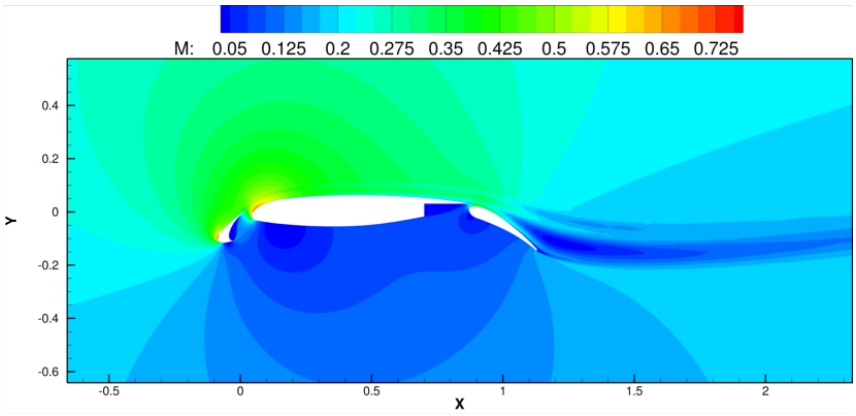

(b) Mach number contours, $p = 3$

Figure 15. Computed Mach number contours using the Spalart-Allmaras turbulence model for flow over the 30P30N multi-element airfoil configuration with $p = 1$ and $p = 3$, $M_\infty = .2$, $\alpha = 16^o$, and $Re = 9,000,000$ using discretization order $p = 1$ to $p = 3$ for the mean flow and a first-order discretization for the turbulence model.

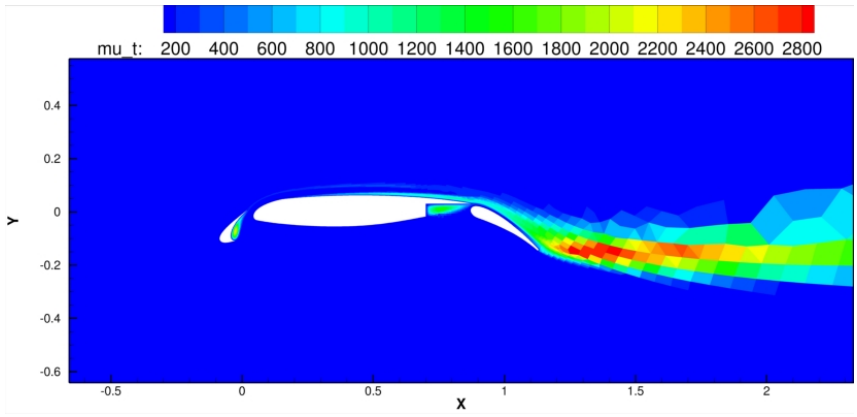

(a) $\rho\tilde{\nu}/\mu_\infty$, $p = 1$

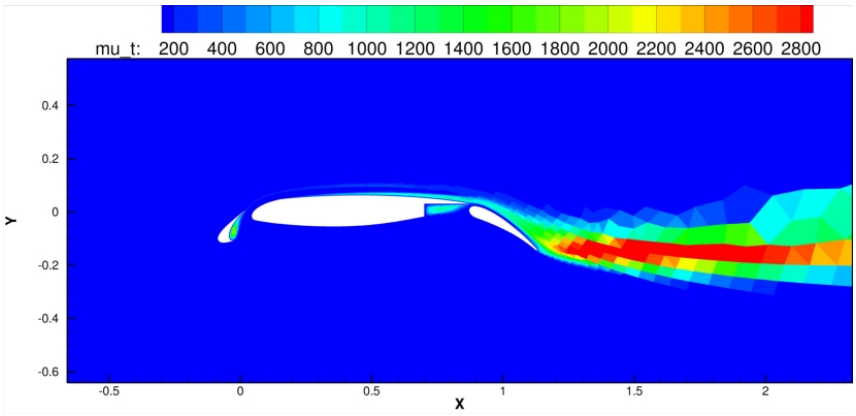

(b) $\rho\tilde{\nu}/\mu_\infty$, $p = 3$

Figure 16. Computed $\rho\tilde{\nu}/\mu_\infty$ contours using the Spalart-Allmaras turbulence model for flow over the 30P30N multi-element airfoil configuration airfoil with $p = 1$ and $p = 3$, $M_\infty = .2$, $\alpha = 16^o$, and $Re = 9,000,000$ using mean flow discretization orders $p = 1$ to $p = 3$ and a first-order discretization for the turbulence model.

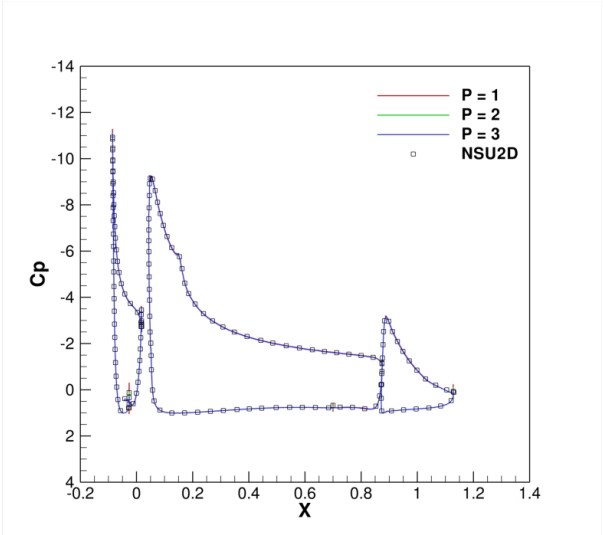

(a) Surface pressure coefficient $p = 1$ to $p = 3$

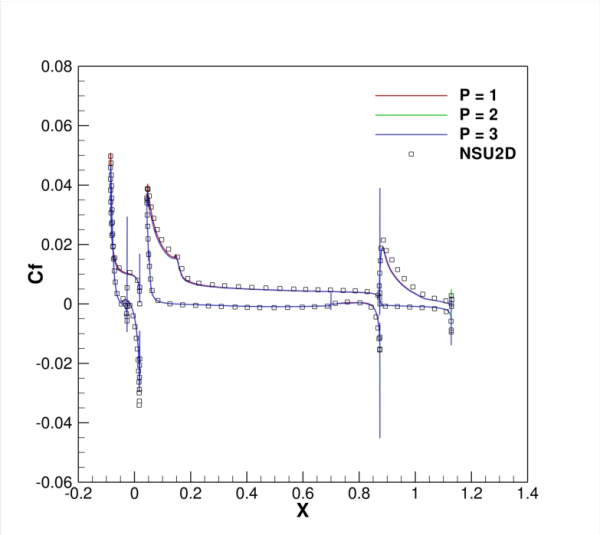

(b) Skin friction coefficient $p = 1$ to $p = 3$

Figure 17. Computed surface pressure and skin friction coefficients using the Spalart-Allmaras turbulence model for flow over the 30P30N multi-element airfoil configuration with mean flow discretization orders $p = 1$ and $p = 3$ at $M_\infty = .2$, $\alpha = 16^o$, and $Re = 9,000,000$.

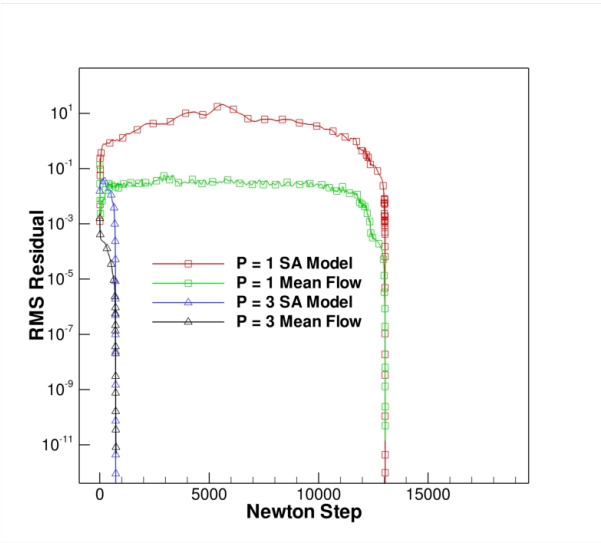

Figure 18. Convergence history for flow over the 30P30N multi-element airfoil configuration using the Spalart-Allmaras turbulence model at $M_\infty = .2$, $\alpha = 16^o$, and $Re = 9,000,000$ using mean flow discretization orders $p = 1$ and $p = 3$.

The Mach number and normalized turbulence model working variable contours for $p = 1$ and $p = 3$ solutions are depicted in Figure 15(a) through Figure 16(b) respectively. This flow is also computed using the NSU2D flow solver, which was previously used to compute this case in reference.[28] The NSU2D flow solver is based on a vertex-centered second-order accurate finite-volume discretization for the mean flow equations and the same first-order accurate finite-volume discretization of the SA turbulence model equation. The NSU2D solver is used to compute the same flow using a triangular unstructured mesh with 250,000 nodes, which is equivalent to 250,000 DoFs. The computed surface pressure and skin friction coefficients using both the present DG solver and the NSU2D solver are depicted in Figure 17(a) and Figure 17(b) respectively. Figure 17(a) and Figure 17(b) show good agreement between the two solvers for both the computed surface pressure coefficient and skin fiction coefficient. There is however, a slight discrepancy in the computed skin friction coefficient on the flap upper surface.

Table 3. Computed lift and drag coefficients for the 30P30N multi-element airfoil configuration using mean flow discretization orders $p = 1$ to $p = 3$.

p	NDoF	C_L	C_D
1	195,899	4.122892	.05293269
2	419,805	4.102815	.05220214
3	727,682	4.103688	.05210565

Table 3 gives the discretization order p, N_{DoF}, computed lift and computed drag coefficients for this case. One can see a regular decrease of the computed drag coefficient as the discretization order is increased. The computed drag coefficient is resolved to within 1 count. The computed lift coefficient varies non-monotonically as the discretization order p is increased and is resolved to approximately 8 counts.

This flow involves strong but smooth flow field gradients and is considered relatively challenging. As such, this case is a good test of the robustness of the proposed approach. The DG discretization of the mean flow equations causes no robustness problems for this case. Figure 18 depicts the iterative convergence of the flow solver and similarly to the previous test cases , once the turbulence model transient has passed the solution converges rapidly to steady-state. Also notice that for the higher-order DG discretizations of the mean equations, the turbulence model transient is far more benign due to the flow solution initialization from a lower-order solution and the fact that the turbulence model resolution remains unchanged during p-enrichment.

VI.D. High-lift Multi-element Airfoil Configuration 30P30N: hp-adaptation

Since the previous hybrid discretization results do not increase turbulence model resolution as the discretization order is increased, an hp-adaptation strategy is employed in order to study the effects of increasing turbulence model resolution in regions of the domain where the turbulence model discretization error is dominant. This test case consists of computing the flow over the 30P30N multi-element airfoil configuration using a lift-driven adjoint-based hp-adaptation

strategy.[16,27] This configuration is the same multi-element airfoil configuration considered in Section VI.C. The flow conditions are $M_\infty = .2$, $\alpha = 16^o$, and $Re = 9,000,000$, as in Section VI.C. In this case the hp-adaptation algorithm is slightly modified to accommodate the finite-volume discretization of the turbulence model. The computable error estimate[16,27] can be broken up into contributions from the different PDEs in the system by taking the inner product over the modal coefficients separately for each field in the system of equations. When the contribution to the total error from the turbulence model equation exceeds 50% of the total error for an element, the element is flagged for h-refinement regardless of smoothness. This is designed to target the contribution of the turbulence model discretization error to the functional error estimate with h-refinement, since the standard hp-adaptive approach might otherwise employ p-enrichment everywhere because the mean flow is smooth and the turbulence model smoothness is irrelevant due to the first-order accurate discretization.

Figure 19(a) depicts the initial mesh containing $N = 55,964$ elements with a discretization order $p = 1$. Figure

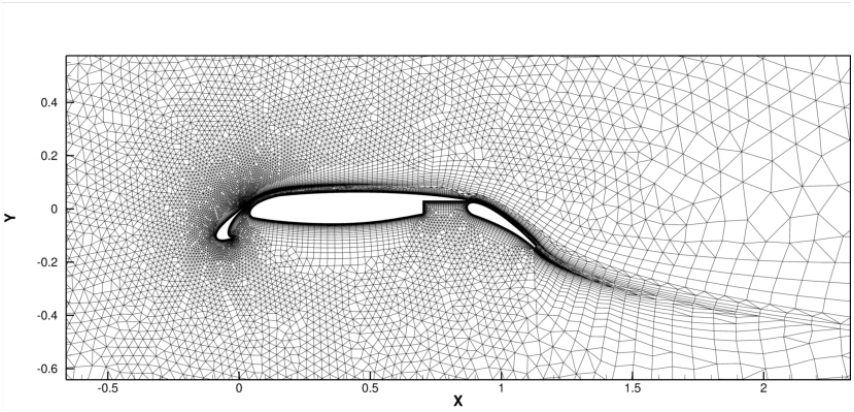

(a) Initial mesh: $N = 55,964$ and $p = 1$

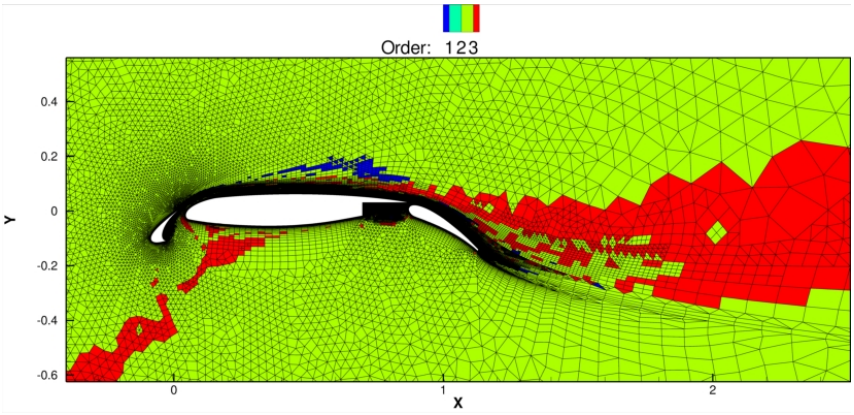

(b) Final mesh: $N = 536,261$ and $p = 1$ to $p = 3$

Figure 19. Unstructured mixed-element meshes used for computing flow around the 30P30N high-lift multi-element airfoil configuration at $M_\infty = .2$, $\alpha = 16^o$, and $Re = 9,000,000$ using hp-adaptation.

19(b) depicts the final hp-adapted mesh, which is refined using h-refinement in regions where the turbulence model discretization error is the dominant source of the lift error estimate. Figure 20(a) shows the mesh and discretization order in the flap cove region on the final hp-adapted mesh. Aggressive mesh refinement is applied in this region due to the dominance of turbulence model error contribution to the lift error estimate. Unfortunately the mean flow would benefit from additional p-enrichment in this region due to the purely smooth reverse flow behavior as shown in Figure 20(b).

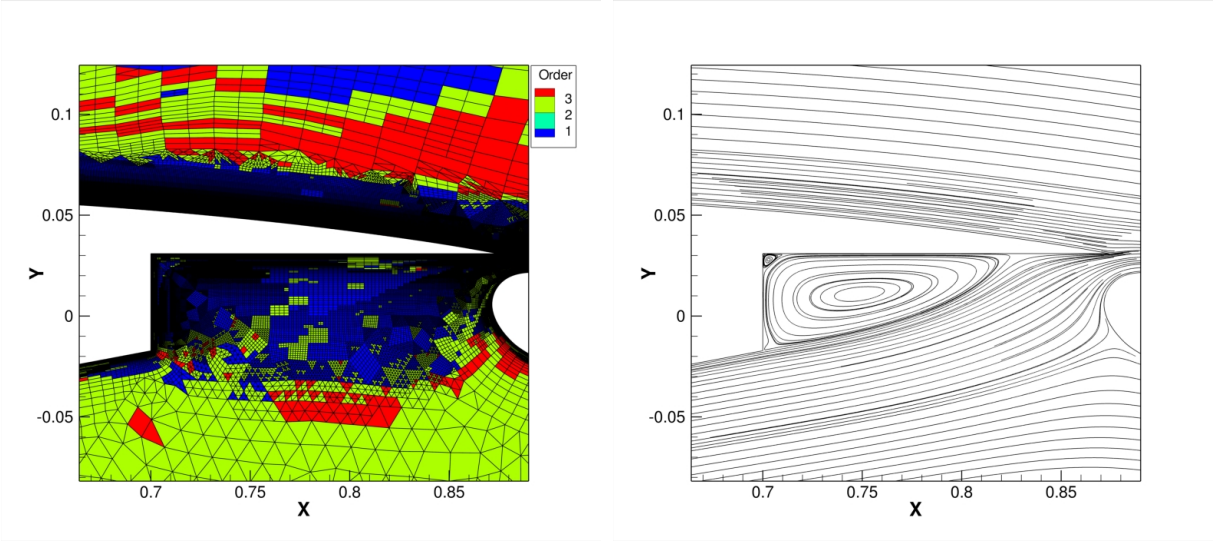

(a) Close-up of flap cove mesh

(b) Streamlines in flap cove

Figure 20. Close-up of the mesh and stream lines in the flap cove on the final hp-adapted mesh for the flow around the 30P30N high-lift multi-element airfoil configuration at $M_\infty = .2$, $\alpha = 16^o$, and $Re = 9,000,000$.

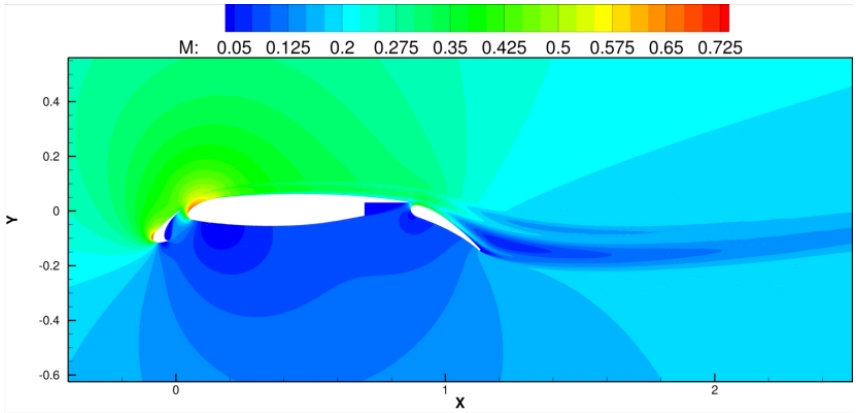

(a) Final Mesh: Mach contours

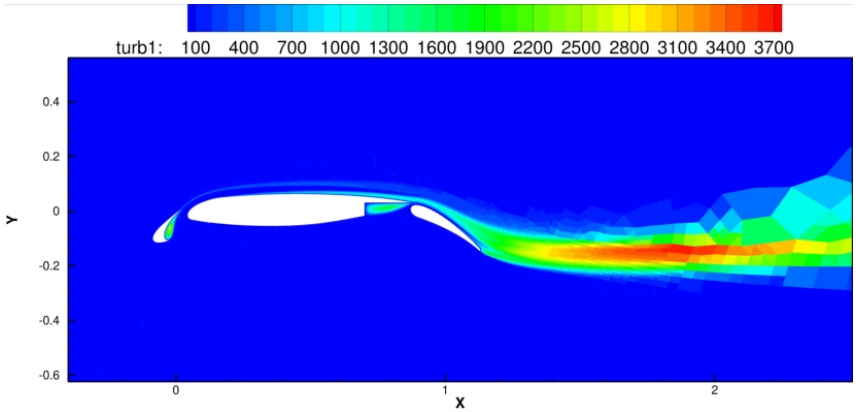

(b) Final Mesh: $\frac{\rho\tilde{\nu}}{\mu_\infty}$ contours

Figure 21. Computed Mach number and eddy viscosity contours on the final hp-adapted mesh for the flow around the 30P30N high-lift multi-element airfoil configuration at $M_\infty = .2$, $\alpha = 16^o$, and $Re = 9,000,000$.

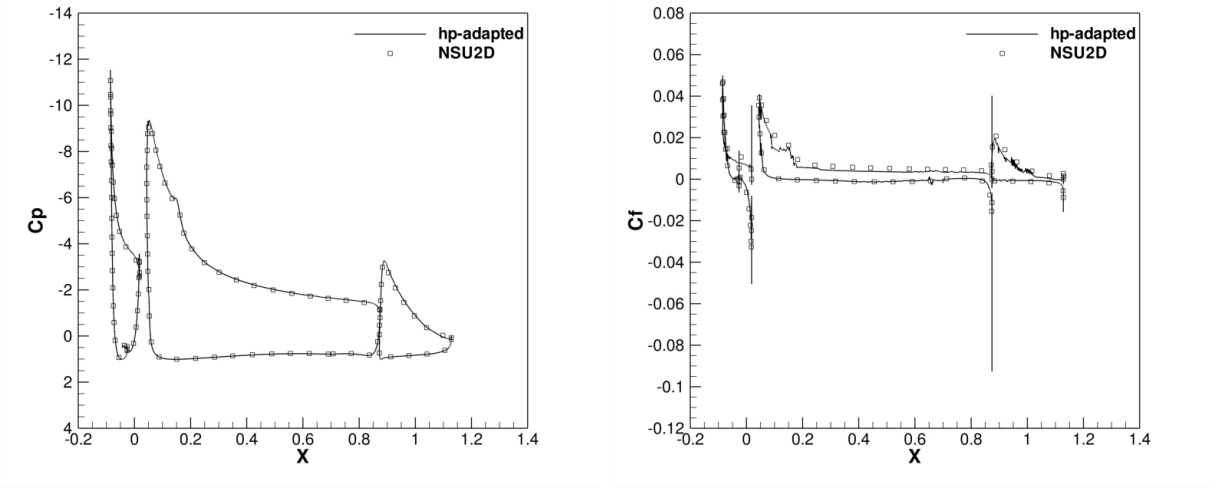

(a) Final mesh: Surface Pressure

(b) Final mesh:Skin Friction

Figure 22. Computed surface pressure and skin friction coefficients on the final hp-adapted mesh for turbulent flow over the 30P30N high-lift multi-element airfoil configuration at $M_\infty = .2$, $\alpha = 16^o$, and $Re = 9,000,000$.

In general the part of the flow that is external to the boundary layer and the wake is refined using p-enrichment, since in these regions the turbulence model influence on the solution is minimal. The hp-adaptive procedure is initialized with the $p = 1$ solution shown in Figure 15(a) and Figure 16(a). Figure 21(a) shows the computed Mach number contours on the final hp-adapted mesh and Figure 21(b) shows the eddy viscosity contours on the final mesh. Clearly hp-adaptation has added significant resolution to the discretizations of both the mean flow and turbulence model equations. As with the previous hybrid discretization results, this solution maintains positive values of the turbulence model working variable throughout the entire domain. As with the uniform p-enrichment case, the DG solver handles the high mean flow gradients without artificial viscosity or limitation.

Figure 22(a) shows the computed surface pressure distribution on the final hp-adapted mesh compared with the results obtained by the NSU2D flow solver. Figure 22(a) shows good agreement in the computed surface pressures obtained with both solvers. Furthermore, the computed surface pressure profile obtained using the DG solver is smooth. Figure 22(b) shows the computed surface skin friction profile compared with the NSU2D flow solver. In this case reasonable agreement of the computed skin friction profile between the two solvers is also obtained. However, the computed skin friction coefficient result obtained by the DG solver is significantly less smooth than the computed skin friction profile obtained by NSU2D. Furthermore, comparing Figure 22(b) to Figure 17(b) shows that the hp-adapted computed skin friction coefficient is significantly less smooth than the computed skin friction coefficient obtained using uniform p-enrichment. The noise in the computed skin friction profile is the result of the contribution of the turbulence model discretization error to the lift error estimate being sufficiently high in some regions that p-enrichment of the flow is prevented in an area where the mean flow would benefit from p-enrichment. One such region is the leading edge of the main element as shown in Figure 23, where the elements next to the wall employ a discretization order of $p = 1$ for the mean flow.

The computed lift and drag coefficient histories over the hp-adaptation process are shown in Figure 24(a) and Figure 24(b) respectively. In addition to the hp-adaptation histories, the uniform p-enrichment computed lift and drag coefficient histories are also shown. Both the computed lift and drag coefficients approach fixed values. Unfortunately the number of unknowns employed for the hp-adapted computation is very high, over 2 million in this case. The high number of unknowns employed is due to the first-order accurate discretization of the turbulence model equation and as such true grid convergence is beyond the computational budget available. Furthermore, comparison between the hp-adapted and uniformly p-enriched results shows the computed lift and drag coefficients are approaching two different values for each refinement method respectively. The two refinement strategies converge to different computed lift and drag coefficients because while hp-adaptation increases the turbulence model resolution, p-enrichment fixes the turbulence model resolution at the number elements in the initial mesh. Clearly the turbulence model resolution has a significant impact on the computed lift and drag coefficient results for this case.

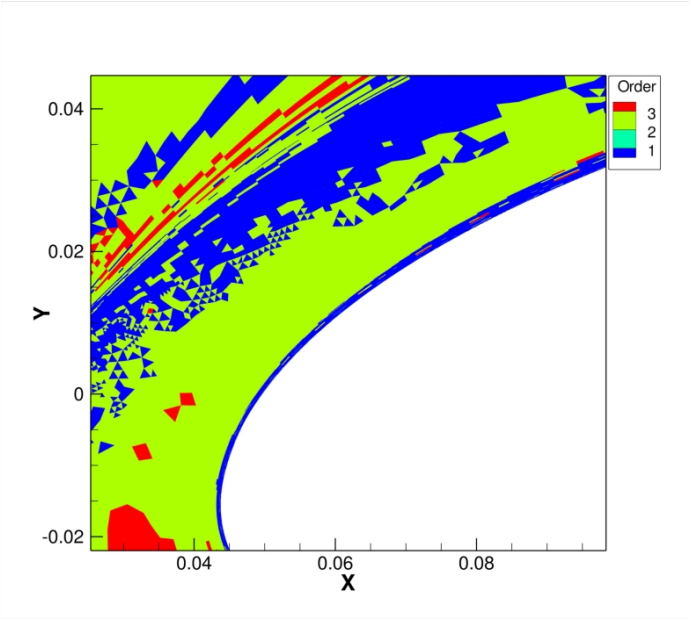

Figure 23. Close-up of order distribution at the nose of the main element of 30P30N high-lift multi-element airfoil configuration. Note that the elements in the boundary layer near the wall employ a discretization order of $p = 1$.

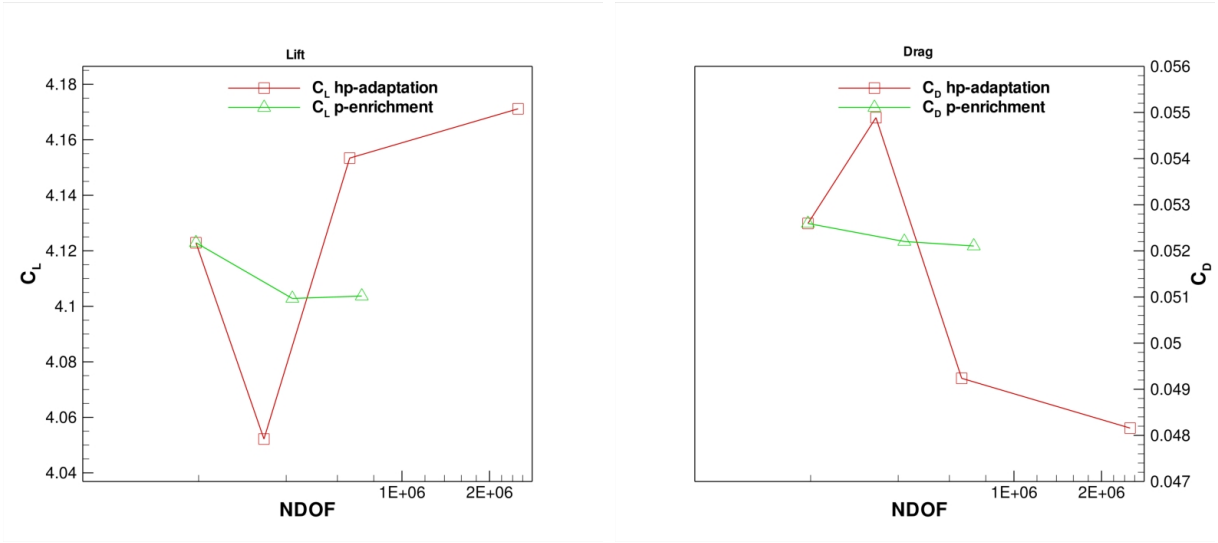

(a) Computed Lift Coefficient

(b) Computed Drag Coefficient

Figure 24. Computed lift and drag coefficients history during adaptation of the flow around the 30P30N high lift configuration at $M_\infty = .2$, $\alpha = 16^o$, and $Re = 9,000,000$.

VII. Numerical Results: DG Discretization of RANS and Modified SA Turbulence Model

In order to asses the robustness enhancement of the SA turbulence model equation modifications discussed in Section IV, three test cases are considered, two of which were also computed using the hybrid discretization approach. For these test cases the modified SA turbulence model equation is discretized using high-order DG discretizations to the same order as the mean flow. Furthermore, a fully coupled Roe approximate Riemann solver[26] is employed for the convective numerical flux of the RANS-SA system for all test cases in this section. All test cases are solved using the fully coupled damped-Newton method with a line-implicit CGS preconditioned GMRES solver as described above and detailed in reference.[27]

VII.A. Subsonic RAE2822 Airfoil

The first test case of the modified SA turbulence model considers the turbulent flow over an RAE2822 airfoil at $M_\infty = .4$, $\alpha = 2.79^o$, and $Re = 6,500,000$. The computational mesh employed for this test case is depicted in Figure 4(a) and is a mixed-element unstructured mesh containing $N = 5,980$ elements, with discretization orders ranging from $p = 1$ to $p = 4$. The solution is converged using the line-implicit CGS preconditioned GMRES Newton solver and each solution of discretization order p is initialized with a fully converged solution of discretization order $p-1$.

The convergence history for this test case is shown in Figure 25(a), which is similar to the hybrid discretization result in Figure 4(b). However, the initial solution takes about 25% more Newton steps to converge the $p = 1$ solution. Furthermore, this convergence history contains none of the secondary transients normally associated with the generation of negative values of $\tilde{\nu}$(see references[10,27]). In fact, qualitatively the convergence behavior of the modified SA turbulence model is very similar to that of the finite-volume discretization of the turbulence model, which is an encouraging result.

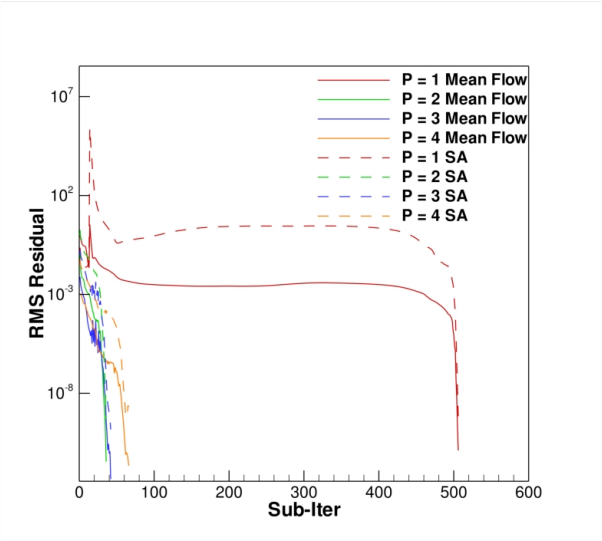

(a) Convergence history

Figure 25. Convergence history for subsonic flow over a RAE2822 airfoil at $M_\infty = .4$, $\alpha = 2.79^o$, and $Re = 6,500,000$ using discretization orders $p = 1$ to $p = 4$ for the mean flow and turbulence model.

Table 4. Computed lift and drag coefficients for the RAE2822 airfoil with $M_\infty = .4$, $\alpha = 2.79^o$, and $Re = 6,500,000$ using $p = 1$ to $p = 4$.

p	NDoF	C_L	C_D
1	21,482	.538653	.010371
2	46,692	.557133	.008982
3	81,548	.557043	.008870
4	126,050	.556914	.008870

Figure 26(a) through Figure 27(b) depict the computed Mach number and eddy viscosity contours for a $p = 1$ and a $p = 4$ discretization respectively. Figure 28(a) illustrates the computed surface pressure distribution for discretization orders $p = 1$ to $p = 4$ and Figure 28(b) shows the computed surface skin friction profiles, also for discretization orders $p = 1$ to $p = 4$. Note that as the discretization order is increased these profiles become smoother indicating that increasing discretization order results in enhanced solution accuracy. Again note that the non-smooth behavior in the computed skin friction profile is located at sharp corners where the geometry is not differentiable.

Table 4 shows the discretization order p, N_{DoF}, computed lift and computed drag coefficients across the discretization order range. Table 4 shows that the computed drag coefficient has been resolved to $< .01$ counts and the computed lift coefficient has been resolved to approximately 1.3 counts. For this test case employing a high-order DG discretization has significantly improved the grid convergence of both the computed lift and drag coefficients. Comparison of Table 4 and Table 1 is another demonstration of the impact of turbulence model resolution on functional outputs. Furthermore, as with the hybrid discretization results in Section VI.A, the lift is not as grid converged as the drag.

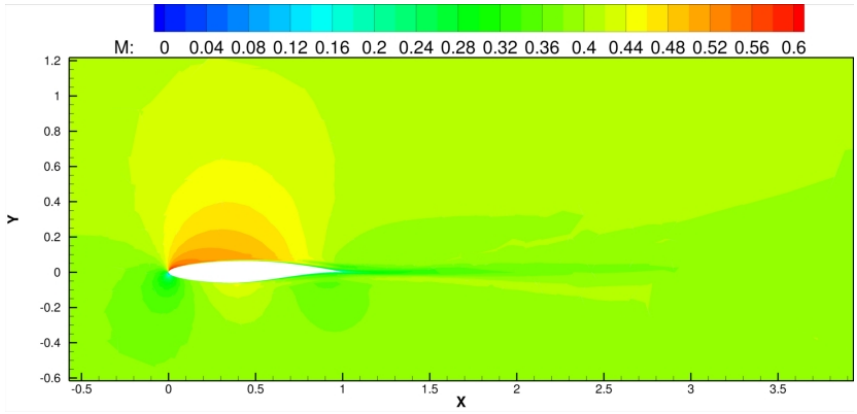

(a) Mach number contours, $p = 1$

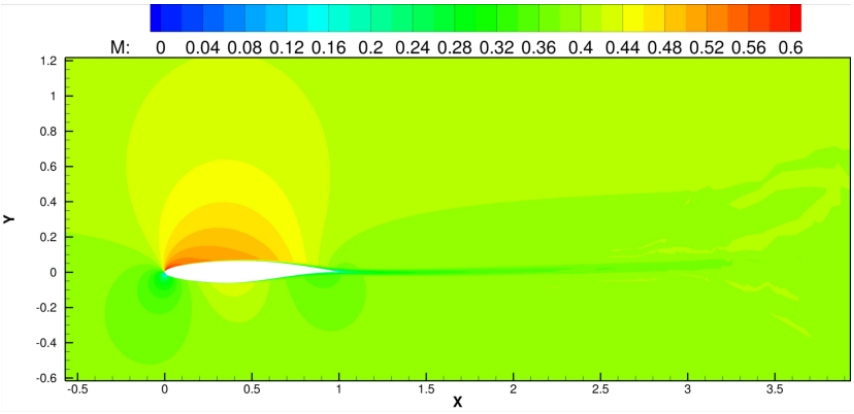

(b) Mach number contours, $p = 4$

Figure 26. Computed Mach number contours for the subsonic flow over an RAE2822 airfoil at $M_\infty = .4$, $\alpha = 2.79^o$, and $Re = 6,500,000$.

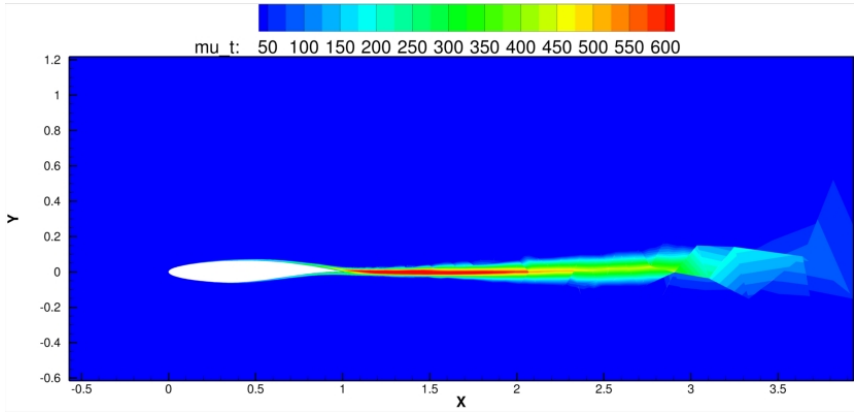

(a) μ_T/μ_∞ contours, $p = 1$

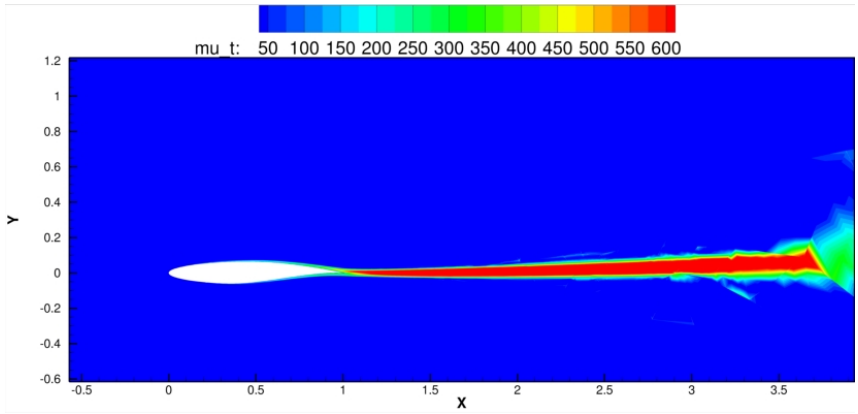

(b) μ_T/μ_∞ contours, $p = 4$

Figure 27. Computed μ_T/μ_∞ contours for subsonic flow over an RAE2822 airfoil using the Spalart Allmaras turbulence model at $M_\infty = .4$, $\alpha = 2.79^o$, and $Re = 6,500,000$ with discretization orders $p = 1$ and $p = 4$.

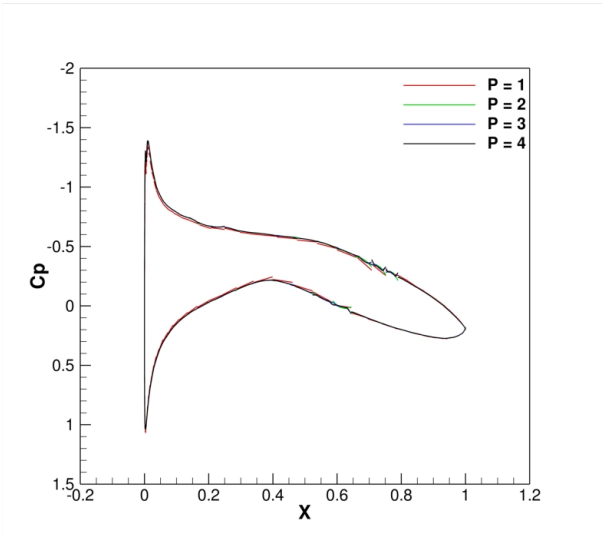

(a) Surface pressure coefficient

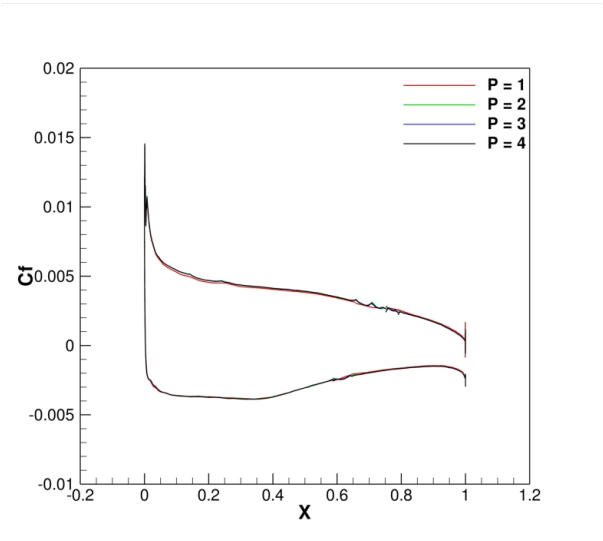

(b) Skin friction coefficient

Figure 28. Computed surface pressure coefficient and skin friction for subsonic flow over an RAE2822 airfoil using the Spalart Allmaras turbulence model at $M_\infty = .4$, $\alpha = 2.79^o$, and $Re = 6,500,000$ using $p = 1$ to $p = 4$.

VII.B. Transonic RAE2822 Airfoil

The second test case of the modified SA turbulence model considers the transonic turbulent flow over an RAE2822 airfoil at $M_\infty = .734$, $\alpha = 2.79^o$, and $Re = 6,500,000$. The computational mesh employed for this test case is a mixed-element unstructured mesh containing $N = 19,607$ elements, depicted in Figure 29(a). The discretization orders range from $p = 1$ to $p = 3$. The solution is converged using a line-implicit CGS preconditioned GMRES solver and each solution of discretization order p is initialized with a fully converged solution of discretization order $p-1$. The shock wave is captured using a piecewise constant artificial viscosity method[16,27,30]

The convergence history for this test case is shown in Figure 29(b), showing a fully converged mean flow and turbulence model solution for all discretization orders.

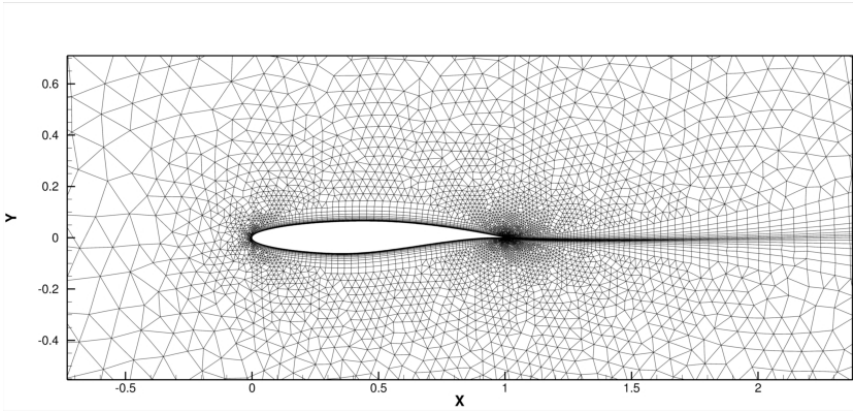

(a) Mesh $N = 19,607$

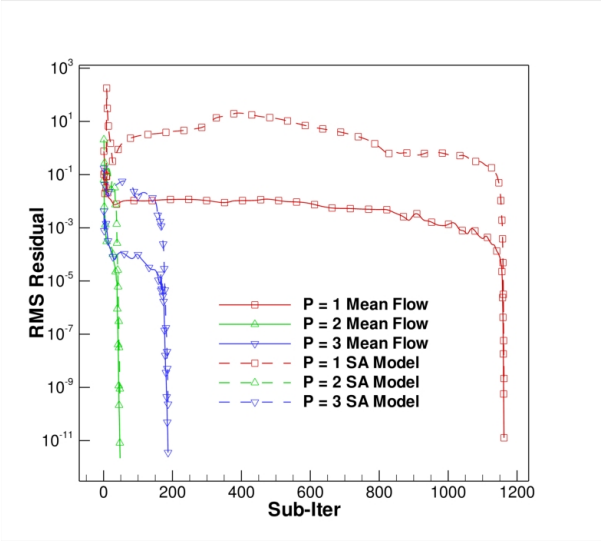

(b) Convergence history

Figure 29. Convergence history for transonic flow over an RAE2822 airfoil at $M_\infty = .734$, $\alpha = 2.79^o$, and $Re = 6,500,000$ using discretization orders $p = 1$ to $p = 3$ for the mean flow and turbulence model.

Table 5. Computed lift and drag coefficients for the RAE2822 airfoil with $M_\infty = .734$, $\alpha = 2.79^o$, and $Re = 6,500,000$ using $p = 1$ to $p = 3$.

p	NDoF	C_L	C_D
1	68,187	.702010	.014071
2	145,740	.710276	.014310
3	252,266	.715421	.014425

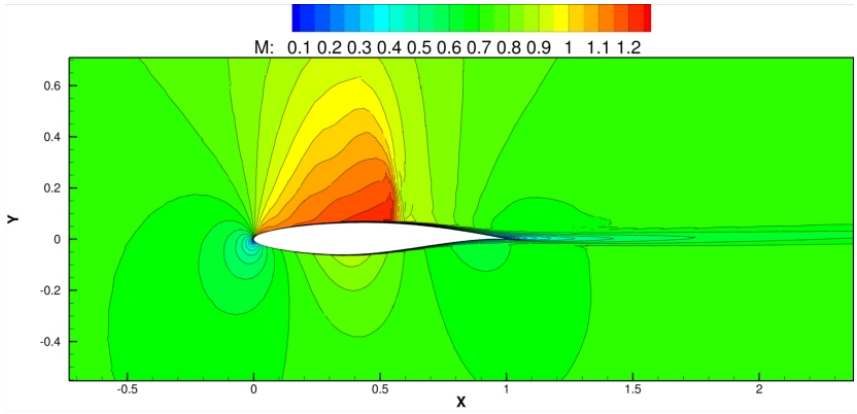

(a) Mach number contours, $p = 1$

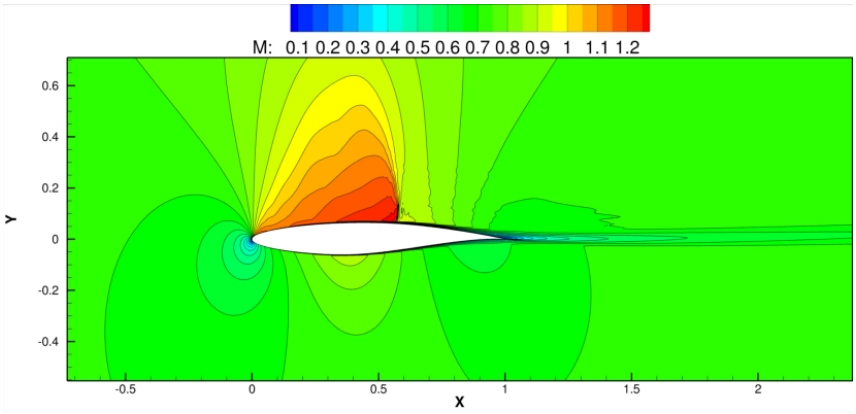

(b) Mach number contours, $p = 3$

Figure 30. Computed Mach number contours for transonic flow over an RAE2822 airfoil at $M_\infty = .734$, $\alpha = 2.79^o$, and $Re = 6,500,000$.

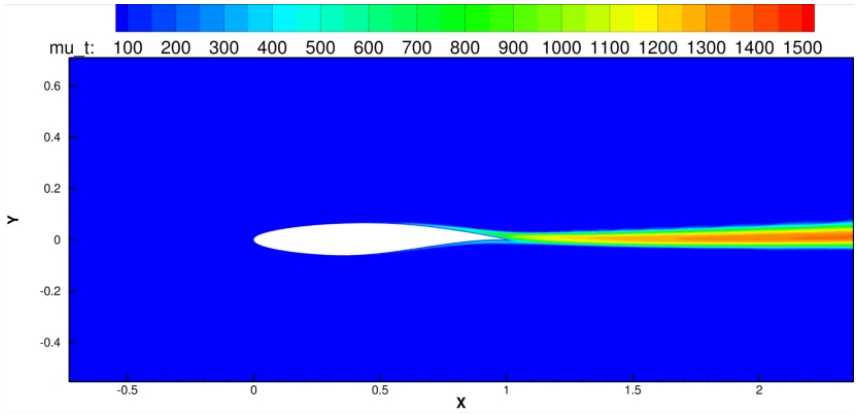

(a) μ_T/μ_∞ contours, $p = 1$

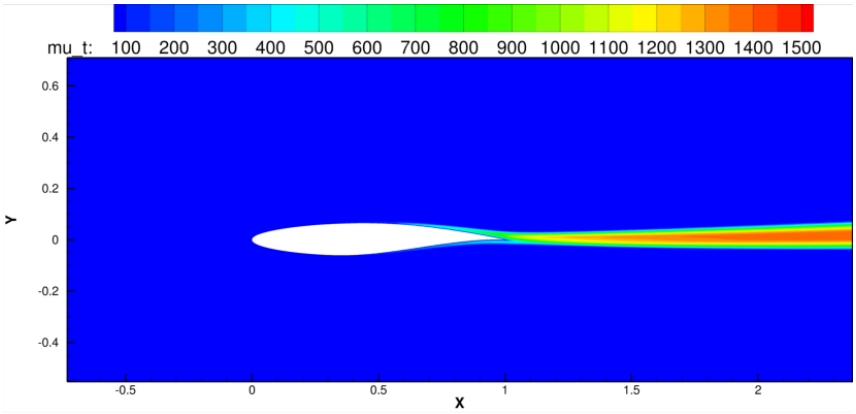

(b) μ_T/μ_∞ contours, $p = 3$

Figure 31. Computed μ_T/μ_∞ contours for transonic flow over an RAE2822 airfoil using the Spalart Allmaras turbulence model at $M_\infty = .734$, $\alpha = 2.79^o$, and $Re = 6,500,000$ with discretization orders $p = 1$ and $p = 3$.

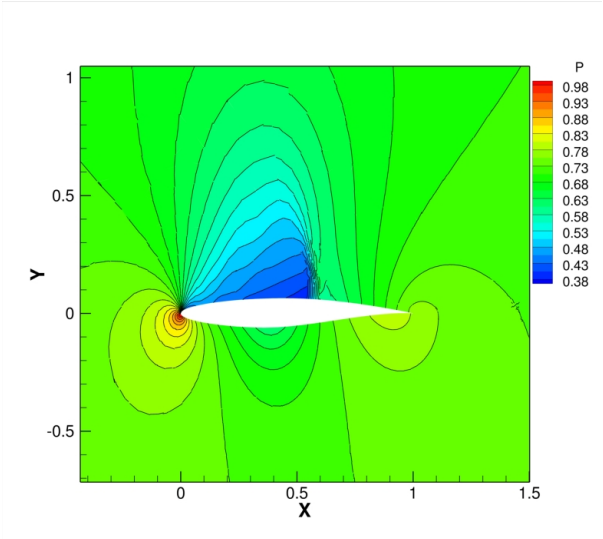

(a) Pressure contours $p = 1$

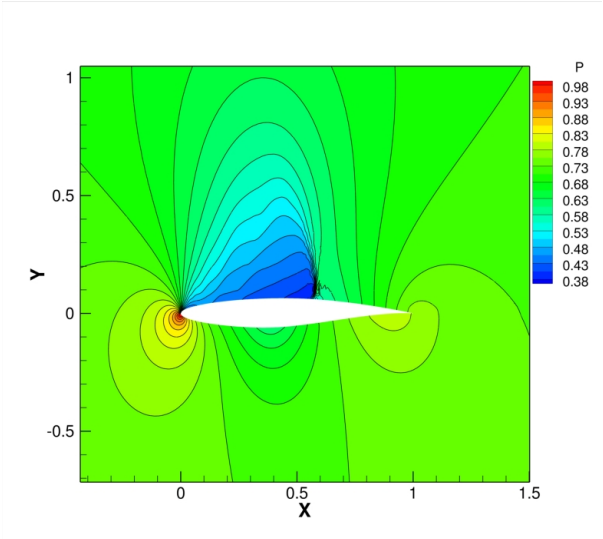

(b) Pressure contours $p = 3$

Figure 32. Computed pressure contours for transonic flow over an RAE2822 airfoil using the Spalart Allmaras turbulence model at $M_\infty = .734$, $\alpha = 2.79^o$, and $Re = 6,500,000$ using $p = 1$ and $p = 3$.

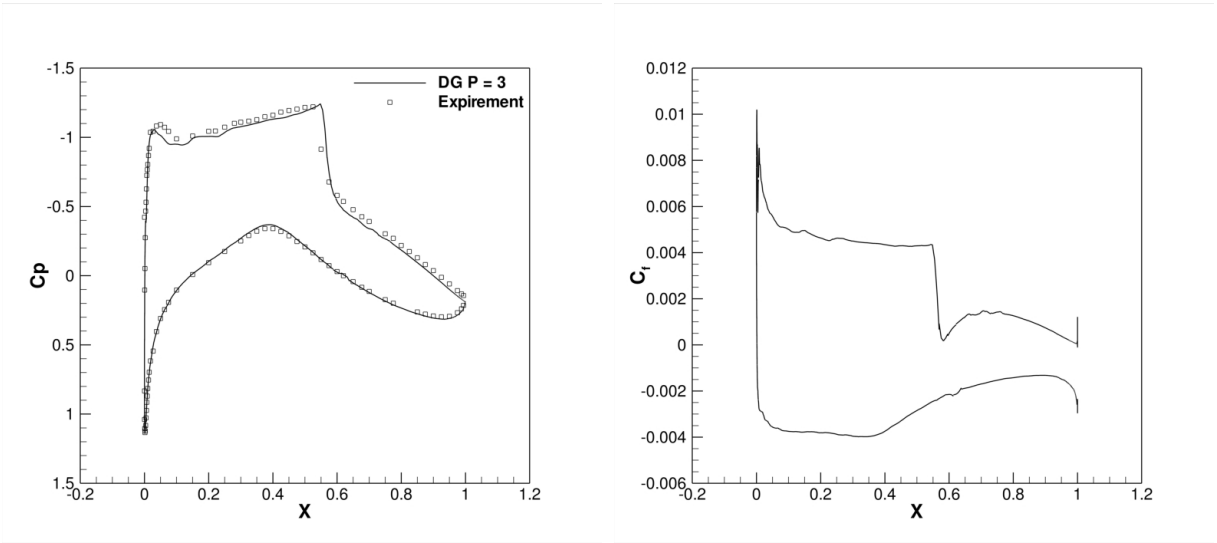

(a) Surface pressure coefficient

(b) Skin friction coefficient

Figure 33. Computed surface pressure coefficient and skin friction for transonic flow over an RAE2822 airfoil using the Spalart Allmaras turbulence model at $M_\infty = .734$, $\alpha = 2.79^o$, and $Re = 6,500,000$ using $p = 3$.

Figure 30(a) through Figure 31(b) depict the computed Mach number and eddy viscosity contours for a $p = 1$ and a $p = 3$ discretization respectively. Figure 32(a) through Figure 32(b) show the computed pressure contours and as the discretization order is increased the shock wave width decreases significantly. Figure 33(a) shows the computed surface pressure distribution for $p = 3$ compared against experiment. Overall the numerical solution compares well with the experimental data. The pre-shock suction pressure as well as the shock wave location compare very well with the experimental results, however the leading edge suction peak is slightly too far forward on the airfoil surface. Figure 33(b) shows the computed surface skin friction profile also for a discretization order of $p = 3$, which is smooth and also depicts a crisply captured shock wave.

Table 5 shows the discretization order p, N_{DoF}, computed lift and computed drag coefficients across the discretization order range. Table 1 shows that for this flow grid convergence is not achieved. This flow is particularly challenging from a grid convergence point of view due to the stabilization requirements imposed by the shock wave. Previous work[16] has demonstrated that p-enrichment is not the optimal refinement method for a flow containing a shock wave and smooth flow features. Therefore, future work will focus on applying improved refinement methods for this test case. The main point of this test case is to demonstrate that the addition of a transonic shock wave does not adversely impact the robustness of the solver beyond requiring some artificial diffusion to stabilize the high-order solution in the presence of shock waves.

VII.C. High Lift Multi-element Airfoil: 30P30N

In the authors' experience some of the most challenging flow problems for high-order DG discretizations of the RANS and turbulence model equations are high-lift multi-element airfoil flows. These flows require a very robust solver for both the turbulence model and mean flow equations. To demonstrate the robustness of the DG solver using the modified SA turbulence model, the flow over the 30P30N high-lift multi-element airfoil configuration is considered. The flow conditions for this test case are $M_\infty = .2$, $\alpha = 16^o$, and $Re = 9,000,000$. The geometry and mesh are described in Section VI.C, which considers the same flow problem using the aforementioned hybrid discretization approach.

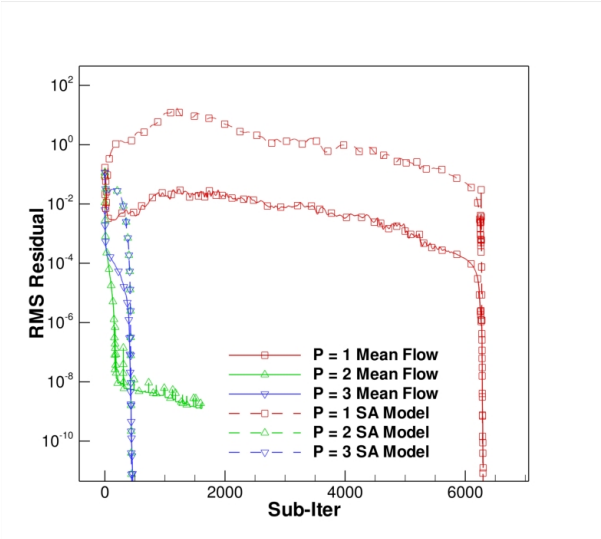

Figure 34. Convergence history for flow over the 30P30N multi-element airfoil configuration using the Spalart-Allmaras turbulence model at $M_\infty = .2$, $\alpha = 16^o$, and $Re = 9,000,000$ for discretization orders $p = 1$ through $p = 3$.

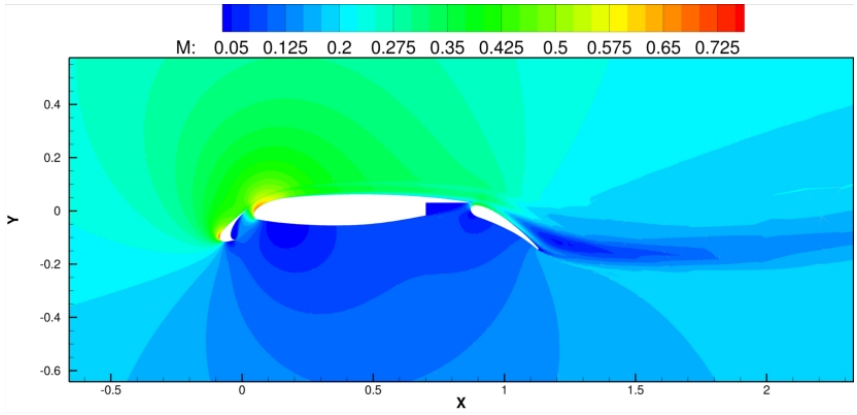

(a) Mach number contours, $p = 1$

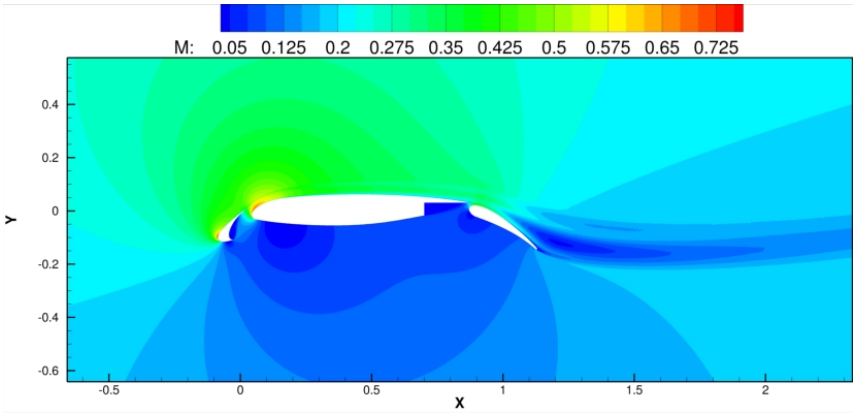

(b) Mach number contours, $p = 4$

Figure 35. Computed Mach number contours using the Spalart-Allmaras turbulence model for flow over the 30P30N multi-element airfoil configuration with, $M_\infty = .2$, $\alpha = 16^o$, and $Re = 9,000,000$ using discretization order $p = 1$ and $p = 4$ for the mean flow and turbulence model.

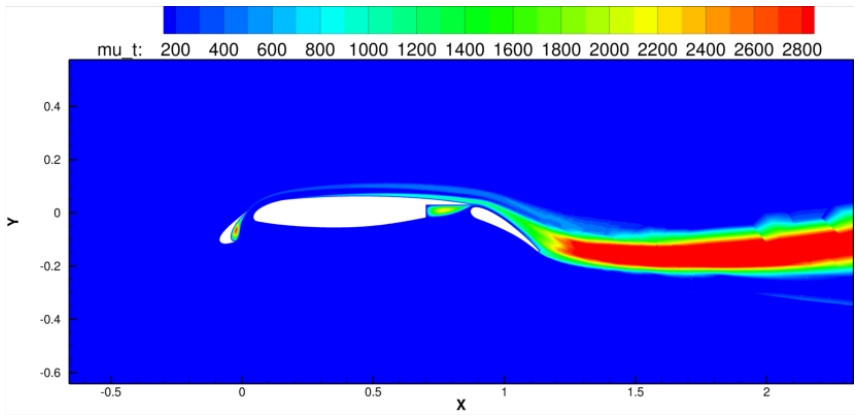

(a) μ_T/μ_∞, $p = 1$

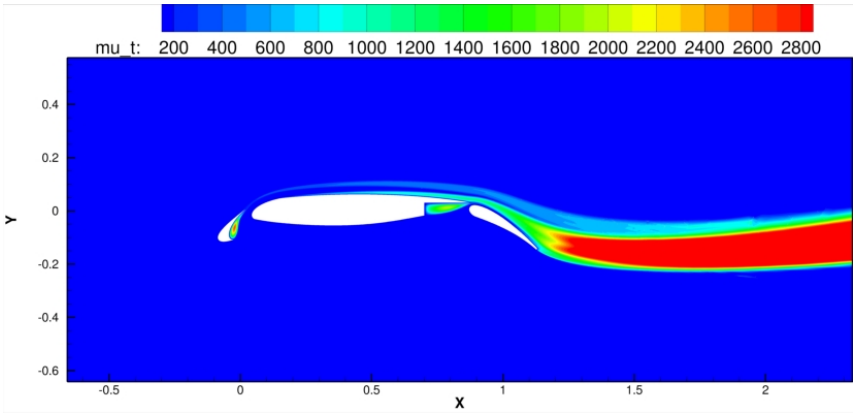

(b) μ_T/μ_∞, $p = 4$

Figure 36. Computed μ_T/μ_∞ contours using the Spalart-Allmaras turbulence model for flow over the 30P30N multi-element airfoil configuration airfoil, $M_\infty = .2$, $\alpha = 16^o$, and $Re = 9,000,000$ using discretization orders $p = 1$ and $p = 4$.

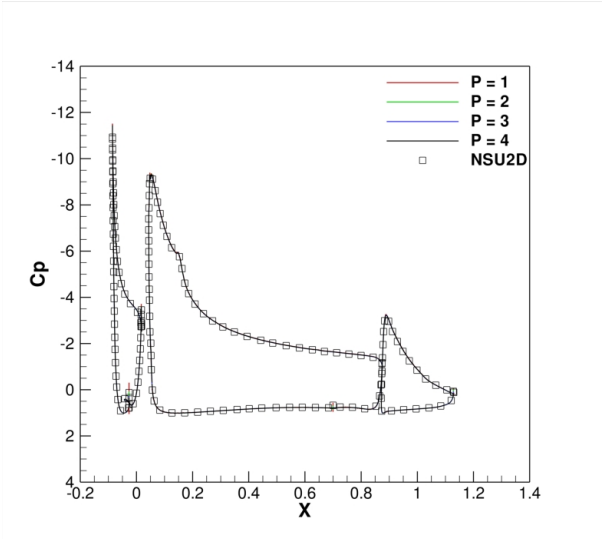

(a) Surface pressure coefficient $p = 1$ to $p = 4$

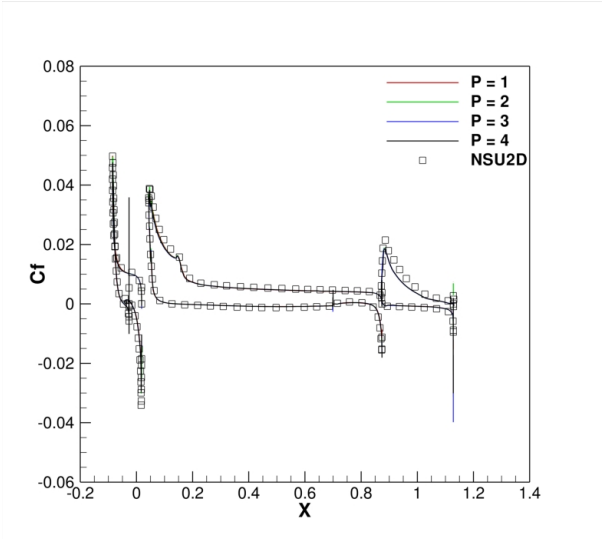

(b) Skin friction coefficient $p = 1$ to $p = 4$

Figure 37. Computed surface pressure and skin friction coefficients using the Spalart-Allmaras turbulence model for flow over the 30P30N multi-element airfoil configuration with discretization orders $p = 1$ to $p = 4$ at $M_\infty = .2$, $\alpha = 16^o$, and $Re = 9,000,000$.

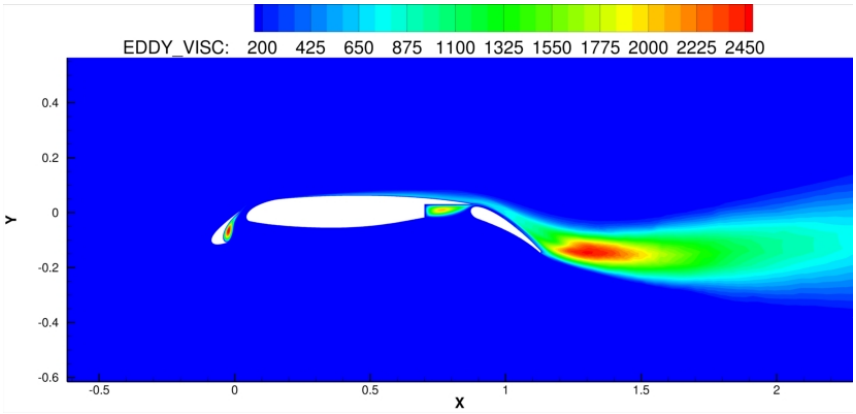

(a) μ_T/μ_∞, NSU2D

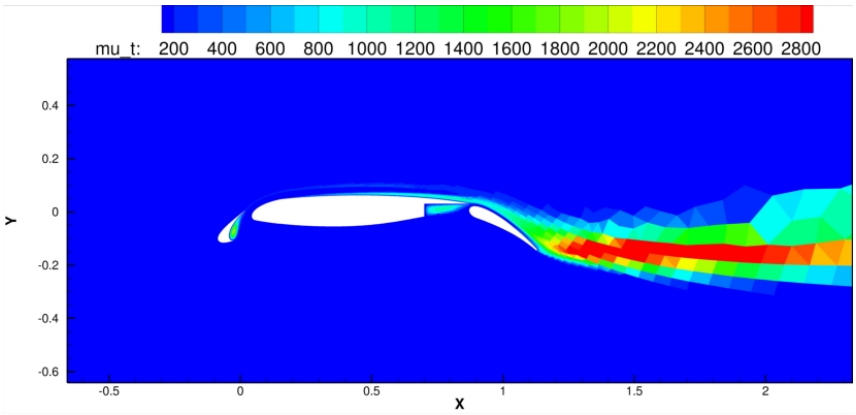

(b) μ_T/μ_∞, hybrid discretization $p = 3$

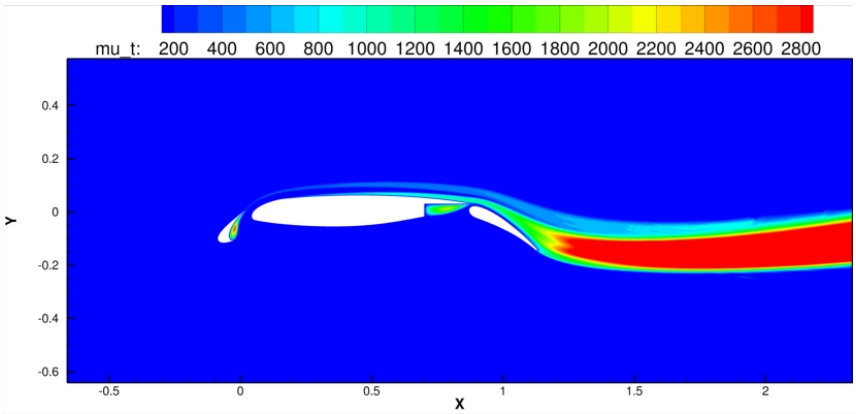

(c) μ_T/μ_∞, $p = 4$

Figure 38. Comparison of μ_T/μ_∞ contours using the Spalart-Allmaras turbulence model for flow over the 30P30N multi-element airfoil configuration airfoil between NSU2D, $p = 3$ hybrid discretization, and $p = 4$ DG discretization.

The convergence history for this test case is shown in Figure 34, demonstrating that a fully converged solution is obtained for both the mean flow and SA turbulence model equations up to a discretization order of $p = 3$. The $p = 4$ results are converged approximately 7 orders of magnitude. We hypothesize that at $p = 4$ minor unsteady flow features are developing in the solution, due to the high resolution and low dissipation of the high-order solution, although further investigation is required validate this assumption. Figure 35(a) through Figure 36(b) show the computed Mach number and turbulent eddy viscosity (μ_T) contours for discretization orders $p = 1$ and $p = 4$. The Mach number contours are qualitatively similar to the hybrid discretization results. However, the eddy viscosity contours illustrate that the DG and finite-volume discretizations of the SA turbulence model equation yield significantly different distributions of the eddy viscosity in the wake region, as seen in Figure 38. The maximum value of the normalized eddy viscosity (μ_T/μ_∞) for the finite-volume discretization is approximately 2800.0 while for the $p = 4$ DG discretization it is approximately 10,224.0. Furthermore, the maximum value of the eddy viscosity is located just downstream from the flap for the finite-volume discretization results, whereas for the DG discretization of the turbulence model the maximum value is located approximately 20 chord lengths downstream from the the flap. The computed eddy viscosity obtained using the NSU2D flow solver (Figure 38(a)) resembles the finite-volume discretization results, which is expected considering that NSU2D uses the same turbulence model discretization.

The computed surface pressure and skin friction coefficients are compared with those obtained using the NSU2D solver as depicted in Figure 37(a) and Figure 37(b) respectively. Figure 37(a) and Figure 37(b) demonstrate that good agreement between the two solvers is obtained using high-order DG discretizations of the turbulence model equation. As with the hybrid discretization results, there is a slight discrepancy in the computed skin friction coefficient on the flap upper surface.

Table 6. Computed lift and drag coefficients for the 30P30N multi-element airfoil configuration using discretization orders $p = 1$ to $p = 4$.

p	NDoF	C_L	C_D
1	195,899	4.163636	.050205
2	419,805	4.154856	.051397
3	727,682	4.154760	.050700
4	1,119,530	4.157237	.052103

Table 6 gives the discretization order p, N_{DoF}, computed lift and computed drag coefficients for this case. Both the computed lift and drag coefficients vary non-monotonically as the discretization order p is increased. From these results it is difficult to judge the grid convergence of the computed lift and drag coefficients. However, the difference between the $p = 3$ and $p = 4$ results is 24 counts of lift and 14 counts of drag. The fact that there is more variation in the force coefficients between the $p = 3$ and $p = 4$ solutions compared to the $p = 2$ and $p = 3$ solutions leads to speculation that additional error may have been incurred due to the incomplete convergence of the $p = 4$ solution.

VIII. Concluding Remarks

Two methods of robustness enhancement have been investigated for a high-order discontinuous Galerkin solver for the Reynolds Averaged Navier-Stokes equations coupled to the turbulence model of Spalart and Allmaras. Each method has been applied to practical aerodynamic test cases, including high-lift multi-element airfoil flows.

The first robustness enhancement method considers discretizing the mean flow equations using high-order DG methods and the turbulence model equation with a low-order finite-volume method. This hybrid discretization method is not necessarily optimal due to the resolution discrepancy between the turbulence model and mean flow discretizations. However, this method has proven to be robust by virtue of the large variety of turbulent flow solutions that have been presented. The hybrid discretization approach mimics a common strategy used in finite-volume and finite-difference methods in order to ensure positivity of the turbulence model discretization. Furthermore, this hybrid discretization has been shown to be capable of obtaining grid converged outputs at fixed turbulence model resolution. However, when the turbulence model resolution is increased changes in functional convergence can be observed. This is indicative of the dependence of simulation outputs to turbulence model resolution and discretization error.

While the hybrid discretization approach is robust, the high-order DG discretization of the modified SA turbulence model in Section IV is equally robust. The modified SA model is advantageous because as the discretization order p is raised the resolution of the mean flow and turbulence model equations are increased simultaneously. Based on the results of Section VI.D, increasing the turbulence model resolution can have a significant impact on simulation outputs. Therefore, employing this modified SA turbulence model appears to be the best choice for solving the RANS equations using high-order DG methods without adverse robustness implications. While the modifications presented

in reference[9] increased the robustness of DG discretizations of the SA turbulence model equation, this work has demonstrated that the additional modification to the $\tilde{S}$ term, as well as a fully coupled convective numerical flux function for the RANS-SA system, and making use of a fully coupled Newton solver, are additional key components for a robust high-order DG solver for turbulent flows.

In spite of these successes, significant work remains in the area of high-order accurate RANS simulations. Firstly, it has been shown that the higher-order turbulence model simulations result in significantly higher eddy viscosity values in wake regions. Although for the test cases presented in this work, the eddy viscosity in wake regions has minimal influence on the results, this may not be the case in more complex three-dimensional problems. Most RANS turbulence models have been developed and calibrated using low-order (first or second-order) accurate discretizations and possible recalibration of the models may be required for use with high-order discretizations. Secondly, although the employed turbulence model modifications result in significantly improved robustness, non-smooth and negative turbulence working variable solutions remain. As pointed out in reference,[27] this non-smooth solution behavior can adversely impact error estimation and the grid convergence of functional outputs, and complicates the use of hp refinement strategies. Therefore, further turbulence model formulation development will be required to address these issues in a high-order methods framework. Although high-order methods are well suited for large-eddy simulations, most practical problems will require the use of hybrid RANS-LES models and the issues discussed herein will remain important for the near-wall RANS portion of these models.

IX. Acknowledgments

This work was supported under AFOSR Grant FA9950-10-C-0051 and NSF Grant 0904936.

References

[1]Cockburn, B. and Shu, C.-W., "Runge-Kutta Discontinuous Galerkin Methods for Convection-Dominated Problems," *SIAM J. Sci. Comput.*, Vol. 16, No. 3, 2001, pp. 173–261.

[2]Wang, L., Mavriplis, D. J., and Anderson, W. K., "Adjoint Sensitivity Formulation for Discontinuous Galerkin Discretizations in Unsteady Inviscid Flow Problems," *AIAA Journal*, Vol. 48, No. 12, Dec 2010, pp. 2867–2883.

[3]Mascarenhas, B. S., Helenbrook, B. T., and Atkins, H. L., "Application of p-Multigrid to Discontinuous Galerkin Formulations of the Euler Equations," *AIAA Journal*, Vol. 47, No. 5, May 2009, pp. 1200–1208.

[4]Bassi, F. and Rebay, S., "Numerical Evaluation of two discontinuous Galerkin methods for the compressible Navier-Stokes equations," *Int. J. Numer. Meth. in Fluids*, Vol. 40, No. 1, Sept 2002, pp. 197–207.

[5]Xia, Y., Luo, H., Norgaliev, R., and Cai, C., "A class of Reconstructed Discontinuous Galerkin Methods for the Compressible Flows on Arbitrary Grids," *Proceedings of the 49th AIAA Aerospace Sciences Meeting, Orlando FL*, jan 2011, AIAA Paper 2011-199.

[6]Shahbazi, K., *A Parallel High-Order Discontinuous Galerkin Solver For The Unsteady Incompressible Navier-Stokes Equations in Complex Geometries*, Ph.D. thesis, University of Toronto, may 2007.

[7]Oliver, T. A. and Darmofal, D. L., "An Unsteady Adaptation Algorithm for Discontinuous Galerkin Discretizations of the RANS Equations," *Proceeding of the 18th AIAA CFD Conference, Miami, FL*, jun 2007, AIAA Paper 2007-3940.

[8]Oliver, T. A. and Darmofal, D. L., "Impact of Turbulence Model Irregularity on High-Order Discretizations," *Proceeding of the 47th Aerospace Sciences Meeting and Exhibit, Orlando FL*, jan 2009, AIAA Paper 2009-953.

[9]Moro, D., Nguyen, N., and Peraire, J., "Navier-Stokes Solution Using Hybridizable Discontinuous Galerkin methods," *Proceeding of the 20th Computational Fluid Dynamics Conference, Honolulu, HW*, Jun 2011, AIAA Paper 2011-3407.

[10]Burgess, N. K., Nastase, C. R., and Mavriplis, D. J., "Efficient Solution Techniques for Discontinuous Galerkin Discretizations of the Navier-Stokes Equations on Hybrid Anisotropic Meshes," *Proceeding of the 48th Aerospace Sciences Meeting, Orlando, FL*, jan 2010, AIAA Paper 2010-1448.

[11]Laflin, K., Brodersen, O., Rakowitz, M., Vassberg, J., Wahls, R., and Morrison, J., "Summary of Data from the Second AIAA CFD Drag Prediction Workshop," AIAA Paper 2004-0555.

[12]Vassberg, J. C., Tinoco, E. N., Mani, M., Brodersen, O. P., Eisfeld, B., Wahls, R. A., Morrison, J. H., Zickuhr, T., Laflin, K. R., and Mavriplis, D. J., "Summary of the Third AIAA CFD Drag Prediction Workshop," AIAA Paper 2007-0260.

[13]Hartmann, R. and Houston, P., "An optimal order interior penalty discontinuous Galerkin discretization of the compressible Navier-Stokes equations," *Journal of Computational Physics*, Vol. 227, No. 22, Nov 2008, pp. 9670–9685.

[14]Wang, L. and Mavriplis, D. J., "Adjoint-based h-p adaptive discontinuous Galerkin methods for the 2D Euler Equations," *Journal of Computational Physics*, Vol. 228, No. 20, Nov 2009, pp. 7643–7661.

[15]Oliver, T. A., *A high-order, adaptive, discontinuous Galerkin finite element method for the Reynolds averaged Navier-Stokes equations*, Ph.D. thesis, Massachusetts Institute of Technology, sept 2008.

[16]Burgess, N. K. and Mavriplis, D. J., "An hp-Adaptive Discontinuous Galerkin Solver for Aerodynamic flows on Mixed-Element Meshes," *Proceeding of the 49th Aerospace Sciences Meeting, Orlando, FL*, jan 2011, AIAA Paper 2011-490.

[17]Leicht, T. and Hartmann, R., "Goal-oriented Error Estimation and hp-Adaptive Mesh Refinement for Aerodynamic Flows," *Proceeding of the 49th Aerospace Sciences Meeting, Orlando, FL*, jan 2011, AIAA Paper 2011-212.

[18]Gao, H. and Wang, Z., "A Residual-Based Procedure for hp-Adaptation on 2D Hybrid Meshes," *Proceeding of the 49th Aerospace Sciences Meeting, Orlando, FL*, jan 2011, AIAA Paper 2011-492.

[19]Bassi, F., Crivellini, A., Rebay, S., and Savini, M., "Discontinuous Galerkin solution of the Reynolds-averaged Navier-Stokes and k-ω turbulence model equations," *Computers and Fluids*, Vol. 34, No. 4, May 2005, pp. 507–540.

[20]Ngoc Cuong Nguyen, P.-O. P. and Peraire, J., "RANS Solutions Using High Order Discontinuous Galerkin Methods," *Proceeding of the 45th Aerospace Sciences Meeting, Reno, NV*, jan 2007, AIAA Paper 2007-914.

[21]Hartmann, R., Held, J., and Leicht, T., "Adjoint-based error estimation and adaptive mesh refinement for the RANS and k-ω turbulence model equations," *Journal of Computational Physics*, Vol. 230, No. 11, May 2011, pp. 4268–4284.

[22]Spalart, P. and Allmaras, S., "A one-equation turbulence model for Aerodynamic flows," *Le Recherche Aerospátiale*, Vol. 1, 1994, pp. 5–21.

[23]Krist, S. L., Biedron, R. T., and Rumsey, C. L., "CFL3D User's Manual (Version 5.0)," NASA Technical Report 1988-208444, NASA, Jun 1998.

[24]Nielsen, E. J., "FUN3D User's Manual," .

[25]Mavriplis, D. J., "Third Drag Prediction Workshop Using the NSU3D Unstructured Mesh Solver," *AIAA Journal of Aircraft*, Vol. 45, No. 3, Mar 2008, pp. 750–761.

[26]Roe, P. L., "Approximate Riemann Solvers, Parameter vectors, and Difference Schemes," *J. Comput. Phys.*, Vol. 43, 1981, pp. 357–372.

[27]Burgess, N. K., *An Adaptive Discontinuous Galerkin Solver for Aerodynamic Flows*, Ph.D. thesis, University of Wyoming, Nov 2011.

[28]Valarezo, W. O. and Mavriplis, D. J., "Navier-Stokes Applications to High-Lift Airfoil Analysis," *AIAA Journal of Aircraft*, Vol. 32, No. 3, May 1995, pp. 618–624.

[29]Mavriplis, D. J., "Revisiting the Least-Squares Procedure for Gradient Reconstruction on Unstructured Meshes," *Proceeding of the 16th Computational Fluid Dynamics Conference, Orlando, FL*, jun 2003, AIAA Paper 2003-3986.

[30]Persson, P.-O. and Peraire, J., "Sub-Cell Shock Capturing for Discontinuous Galerkind Methods," *Proceedings of 44th Aerospace Sciences Meeting and Exhibit, Reno NV*, jan 2006, AIAA Paper 2006-112.